LBL-11664


# Nuclear Structure and Heavy-Ion Fusion*

A series of lectures presented at the XIII International Summer School in Nuclear Physics, September 1980, Mikolajki, Poland

Robert G. Stokstad

Nuclear Science Division
Lawrence Berkeley Laboratory
Berkeley, California 94720
U.S.A.

To be published in Nukleonika

*This work was supported by the Nuclear Physics and Nuclear Sciences Division of the U.S. Department of Energy under contract No. W-7405-ENG-48.

ABSTRACT

A series of lectures is presented on experimental studies of heavy-ion fusion reactions with emphasis on the role of nuclear structure in the fusion mechanism. The experiments considered are of three types. The fusion of lighter heavy ions ($A \lesssim 20$) at subcoulomb energies is studied with in-beam $\gamma$-ray techniques, the subbarrier fusion of $^{16}O$ and $^{40}Ar$ with the isotopes of samarium is detected out of beam by x-radiation from delayed activity, and measurements at very high energies, again for the lighter ions, employ direct particle identification of evaporation residues.

The experimental data are compared with predictions based on the fusion of two spheres with the only degree of freedom being the separation of the centers, and which interact via potentials which vary smoothly with changes in the mass and charge of the projectile and target. The data exhibit large deviations from these systematic predictions. (i) In the case of fusion with the isotopes of samarium, a portion of these deviations can be understood in terms of the changing deformation of the target nucleus, but an additional degree of freedom such as neck formation appears necessary. (ii) The results on $^{10}B + {}^{16}O$ and $^{12}C + {}^{14}N \rightarrow {}^{26}Al$ at high bombarding energies indicate a maximum limiting angular momentum characteristic of the compound nucleus. At lower energies the nuclear structure of the colliding ions seems to affect strongly the cross section for fusion. The relative importance of an entrance channel versus a compound nucleus limitation is not always clear, however, an effective or statistical Yrast line may limit the cross section in some cases

(e.g. in $^{12}C + ^{12}C$) but not in others (new data for $^{10}B + ^{14}N$). (iii) Measurements made at subbarrier energies for a variety of projectile-target combinations in the 1p and 2s - 1d shell also indicate that the valence nucleons can affect the energy dependence for fusion. About half the systems studied so far have structureless excitation functions which follow a standard prediction. The other half exhibit large variations from this prediction. The possible importance of neutron transfer is discussed. The two center shell model appears as a promising approach for gaining a qualitative understanding of these phenomena.

In summary, nuclear structure is seen to be an important factor governing the cross section for fusion in the experiments considered here.

## Table of Contents


I. Introduction ..... 6

II. Models and Methods ..... 7

A. Definitions ..... 7

B. Partial Waves ..... 8

C. Main Assumptions ..... 10

D. Real Potentials and Dissipation ..... 12

E. Methods and Approximations for Calculating $\sigma_{fus}$ ..... 15

F. Nuclear Structure and Microscopic Effects ..... 20

III. Subbarrier Fusion Cross Sections for Light Systems ..... 20

A. Motivation ..... 20

B. Experimental Method ..... 21

C. Systematics ..... 27

1. The Standard Prediction ..... 27

2. *Neutron Transfer* ..... 29

3. Energy Averaged Structure ..... 33

D. Theoretical Approaches ..... 38

1. The Entrance Channel ..... 38

2. The Compound Nucleus ..... 41

IV. The Fusion of Light Systems at High Energies ..... 42

A. Motiviation ..... 42

B. Experimental Method ..... 43

C. Results ..... 59

D. Discussion ..... 60

1. Entrance Channel Models ..... 61

2. Compound Nucleus Models ..... 67

3. Synthesis ..... 72

4. The Low-ℓ Window ..... 73

V. The Effect of Nuclear Deformation ..... 76

A. Motivation ..... 76

B. Experimental Method ..... 78

C. Results ..... 86

D. Discussion ..... 86

E. Section Summary ..... 105

VI. Concluding Remarks ..... 107

VII. Acknowledgements ..... 112

References ..... 114

## I. Introduction

This series of lectures will cover three types of experiments on the fusion of heavy ions. In each case it appears that the nuclear structure of the projectile and target or the evolving compound system affects the cross section for fusion in a different manner.

The remarkable feature of the fusion of heavy nuclei (indeed a complex process, from the microscopic point of view) is that we can parametize its gross features rather simply. This fact, taken alone, might suggest that fusion tells us little. However, measurements have been extended and refined in the past decade, and in almost every case, have revealed deviations from the gross features which are sizeable and have significant implications for nuclear structure. Our understanding of nuclear sturcture's role in fusion is still at a rather qualitative level. We are far from the stage of measuring a fusion cross section and deducing from it, through knowledge of the reaction mechanism, quantitative information on nuclear structure. The objective is thus to discover how nuclear structure affects a particular reaction mechanisim, fusion. In pursuit of this we will draw freely on the knowledge obtained from the study of other types of reactions (elastic and inelastic scattering, coulomb excitation, fission), from spectroscopy and, of course, from theory.

There may also be a number of positive side effects accruing from our efforts to understand the reaction mechanism. Fusion is the sine qua non for producing many heavy nuclei whose structure we wish to study (see the lectures by R. M. Diamond, S. Vigdor, E. Roekel and

N. Cindro). In a broader sense, fusion is responsible for the generation of energy in stars, has produced (in stellar explosions) the elements which make up the solar system, and may even prove to be a controlled source of energy in the next century. We hope that an eventual understanding of the relationship of nuclear structure and heavy-ion fusion will make contributions extending beyond the narrow limits confining these lectures.

The three types of experiments to be discussed are:[†]

(i) a series of fusion excitation functions for light ions (e.g. Be, B, C, N, O) fusing with comparable mass targets. The bombarding energies extend as far as possible below the barrier.

(ii) measurements for a selected number of the above systems (e.g. C+N, B+O, N+B) extended to energies as far as possible above the barrier.

(iii) a study of the fusion of $^{16}O$ and $^{40}Ar$ with the spherical and deformed isotopes of a rare earth element, Sm.

A brief description of the different experimental techniques used in each type of measurement will be given. Before embarking, however, it will be useful to consider some general remarks on fusion, what we mean by it, and how we can parametrise and predict it.

## II. Models and Methods

### A. Definitions

The term fusion is sometimes used quite generally to mean any process in which the projectile and target interact strongly such that some degrees of freedom reach equilibration. We wish to be more specific here. Fusion means the complete amalgamation of the target and projectile

[†]The manuscript is not intended to be a review article. With some notable exceptions, the data presented here are drawn mainly from the work of the author and his colleagues (see acknowledgements). While frequent reference is made to other authors, the references cannot be as comprehensive or complete as in a review article.

(i.e. full momentum transfer) to form a compound system which attains complete equilibrium in all degrees of freedom. The only memory the system retains of its formation is through conserved quantities such as mass, charge, energy, angular momentum and, possibly, isospin. Thus, we are talking about Niels Bohr's compound nucleus.

It is one thing to define fusion; it is another matter to verify experimentally that the conditions of the definition have been satisfied. Thus, the meaning of fusion becomes operational, and refers to interactions whose products are consistent with the predictions of models for the decay of equilibrated systems. The Hauser-Feshbach (or statistical) theory of the formation and decay of the compound nucleus is generally used for this purpose.

## B. Partial Waves

The semiclassical nature of heavy ion reactions at non-relativistic energies justifies the approximate classification of reaction mechanisms according to impact parameter, as shown in Fig. 1. Since fusion can occur (classically) only at energies and impact parameters for which the nuclei overlap sufficiently for the nuclear forces to overcome Coulomb repulsion, fusion occurs for the smaller impact parameters.

For all reactions except elastic scattering, we may write

$$\sigma_x = \frac{\pi\lambda^2}{(2S_1+1)(2S_2+1)} \sum_{\ell} \sum_{J} (2J+1) T^x_{\ell,J} \qquad (1)$$

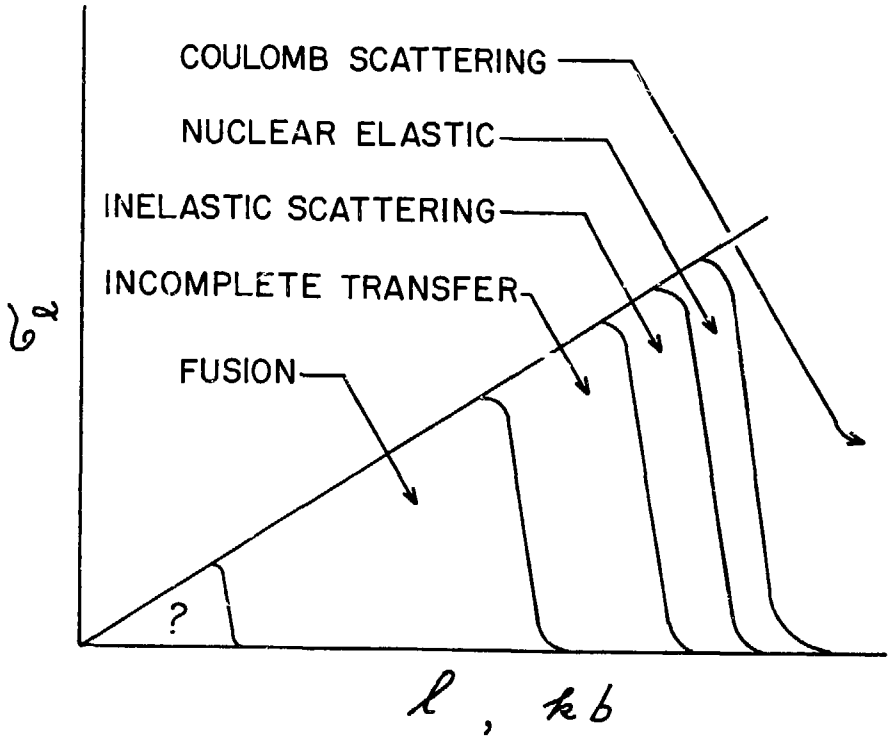


Fig. 1. Schematic classification of nuclear reactions according to the impact parameter b or orbital angular momentum l. The wave number is denoted by k.

where x lables the reaction mechanism (fusion, deep inelastic scattering. transfer etc.), $S_1$ and $S_2$ are the ground state spins of the projectile and target which couple with the orbital angular momentum $\ell$ to produce a total angular momentum J. In most cases (spin zero reactants, $\ell_{max} \gg S_1, S_2$, a negligible spin orbit force) it is sufficient to write.

$$\sigma_x = \pi \lambda^2 \sum_{\ell} (2\ell+1) T_{\ell}^{x} \qquad (2)$$

Models for fusion thus predict the quantify $T_{\ell}^{fus}$, the probability that a given partial wave or impact parameter will fuse.

## C. Main Assumptions

The ingredients of any fusion model are the physical assumptions and approximations which enable one to specify the interaction potential as well as any additional criteria for fusion, if these are not already contained in the potential. These approximations are (usually):

1) spherical symmetry, such that the interaction potential is a function only of the radial separation of the centers of the nuclei. The problem is thus reduced to one dimension. (Refer to Fig. 2. in the following discussion.)

2) the mass parameter associated with the centrifugal degree of freedom is $\mu r^2$ where $\mu = \frac{A_1 A_2}{A_1 + A_2}$. Again, the internal degrees of freedom of the reacting nuclei are suppressed.

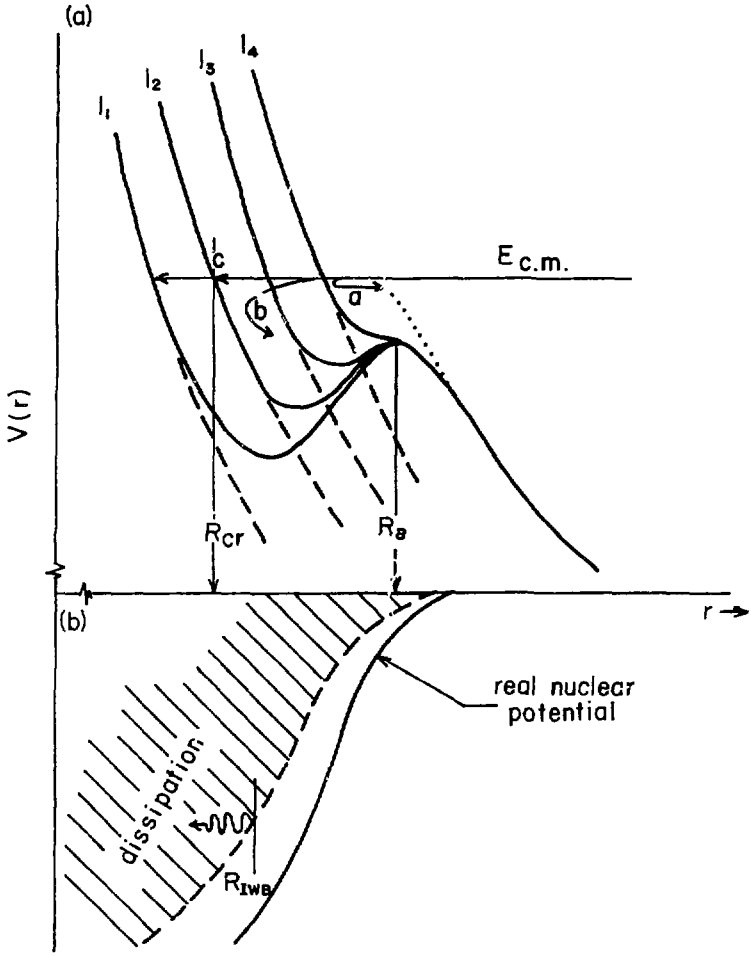


Fig. 2. Schematic illustration of the physical concepts determining fusion cross sections. Fig. 2(a) shows the real nuclear potential for several impact parameters ($\ell_1$-$\ell_4$). The dotted line indicates the Coulomb potential, the dashed lines the centrifugal potentials. Partial wave $\ell_4$ is reflected and does not fuse (orbit a). Partial wave $\ell_3$ is trapped and fuses in a model incorporating dissipation in the region between $R_B$ and $R_{CR}$. This is indicated by orbit b. If penetration to the critical distance $R_{CR}$ is required for fusion, only the partial waves with $\ell \leq \ell_2$ will fuse. At low bombarding energies, quantum mechanical penetration of the interaction barrier $V(R_B)$ will determine the fusion cross section. Another way of effecting absorption is to replace the imaginary potential with an incoming-waves-only boundary condition at $r = R_{IWB}$. (Fig. 2(b)).

D. Real Potentials and Dissipation

The potential describing the interaction of the nuclei is non-conservative. Figure 1 implies that the greater the mass overlap, the stronger the dissipative (or imaginary) portion of the potential. Both the real and the imaginary part of the potential determine whether a given partial wave will fuse.

There are many ways to calculate the nuclear part of the real potential. (This is one avenue by which nuclear structure enters the problem). There are microscopic models (folding,[1] two center shell model[2,3] TDHF[4]) and macroscopic models (liquid drop[5,6]). In the case of microscopic models the interactions sometimes can be calculated from first principles, i.e. from the nucleon-nucleon force.

The imaginary potential is much more difficult to calculate or, in other words, the approximations which must be made are more severe. Because of this the imaginary potential is nearly always treated phenomenologically. Furthermore, practical considerations such as simplicity and computing costs have favored the replacement of the imaginary potential with an ad hoc criterion for the fusion of nuclei interacting only through conservative forces. This criterion can take several forms such as an incoming wave boundary condition[7], a critical angular momentum[5,8] or penetration to a critical radius.[9,10]

One may also solve the classical equations of motion for a potential with disipative terms[11,12], i.e. with radial and tangential friction. Those orbits which become trapped in the pocket of the real potential are associated with fusion. (In the case of very heavy nuclei, this may

not correspond to complete amalgamation of the target and projectile). The dissipative terms are usually phenomenological, although some microscopic estimates of the frictional coefficients have been made.[13]

E. Methods and Approximations for Calculating $\sigma_{fus}$.

Once the model has been specified, there still remain a number of different methods or approximations for obtaining the transmission coefficients, $T_\ell^{fus}$. The most complete way in which this might be done is with the method of coupled channels.[14] Interactions for all processes except fusion would enter explicity into the Hamiltonian, with fusion represented by the imaginary potential. This extreme is not practical, of course, and the degrees of freedom treated explicitly are usually limited to low lying rotational[15] or vibrational excitations and, possibly, giant resonances.

The next step in simplifying the problem is to integrate the Schrödinger equation for a complex potential with no coupled channels. In this case the imaginary potential represents not all inelastic interactions but only those leading to fusion. Although "optical model" codes perform this numerical task, one should not confuse this procedure with the optical model. The potentials in the latter case should reproduce elastic scattering, and the absorption cross section is the total reaction cross section, not necessarily $\sigma_{fus}$.

Because of the additional free parameters associated with a phenomenological representation of the imaginary potential, many authors have chosen to localise the imaginary potential within the classically forbidden region of the real potential ($r < r_i$, Fig. 3) and to assume

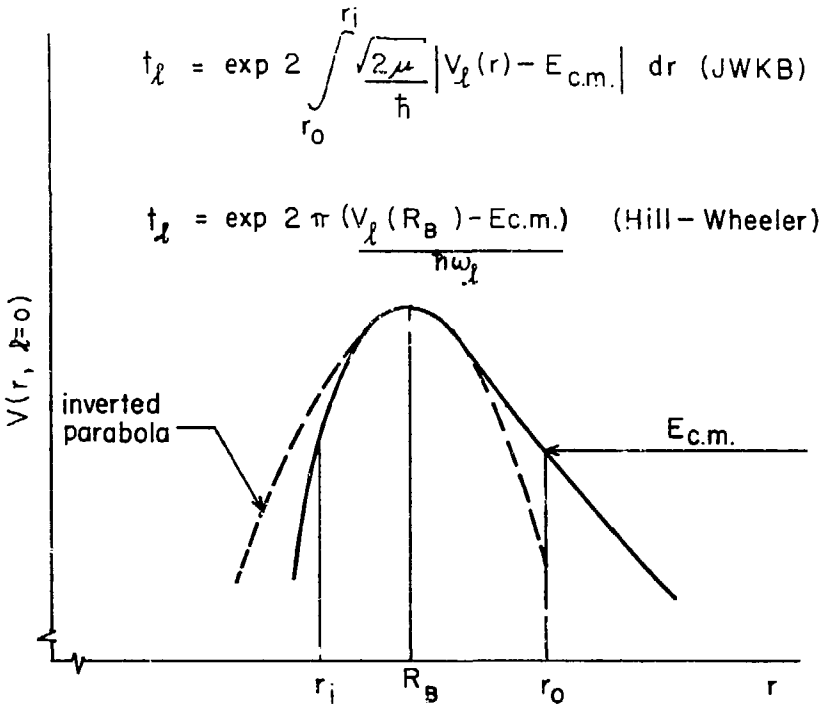


Fig. 5. The JWKB approximation for the calculation of fusion cross sections. The transmission coefficient $T_\ell = (1 + t_\ell)^{-1}$ is obtained under the assumption that complete absorption occurs in the interior region, $r < r_i$. For energies near the barrier, the potential can be approximated by an inverted parabola, in which case the Hill-Wheeler expression applies.

complete absorption in this region. With this incoming-waves-only boundary condition, the real potential completely specfies the problem. Similar to this is the JWKB approximation in which $T_\ell^{fus}$ is given by.

$$T_\ell^{fus} = \frac{1}{1+t_\ell}$$
$$t_\ell = \exp 2\int_{r_o}^{r_i} \sqrt{\frac{2\mu}{\hbar}} \, |V_\ell(r)-E_{c.m.}|^{1/2} \, dr \, . \tag{3}$$

All of these approximations still involve an integral which must be evaluated in general by numerical methods. If the shape of the potential can be approximated by an inverted parabola, then the Hill-Wheeler expression applies

$$t_\ell = \exp 2\pi \frac{(V_\ell(r_{max})-E_{c.m.})}{\hbar\omega_\ell} \tag{4}$$

where

$$\hbar\omega_\ell = \left| \frac{\hbar^2}{\mu} \frac{d^2V_\ell(r)}{dr^2} \right|^{\frac{1}{2}}_{r=r_{max}} \, . \tag{5}$$

Often, the change in the location of the barrier with $\ell$ is neglected, and $r_{max} = R_B$. As indicated qualitatively in Fig. 3 and quantatively in Fig. 4 for a number of systems,[16] the parabolic approximation is good in regions near and above the barrier. At subbarrier energies, it will give transmission coefficients (and hence cross sections) which are relatively too large, since the parabolic barrier is too thin. Equations 3 through 5 and Fig. 3 do illustrate that the fusion cross section in the vicinity of the barrier can be parametrised in terms of three independent quantities, the height of the S-wave barrier, the "curvature"

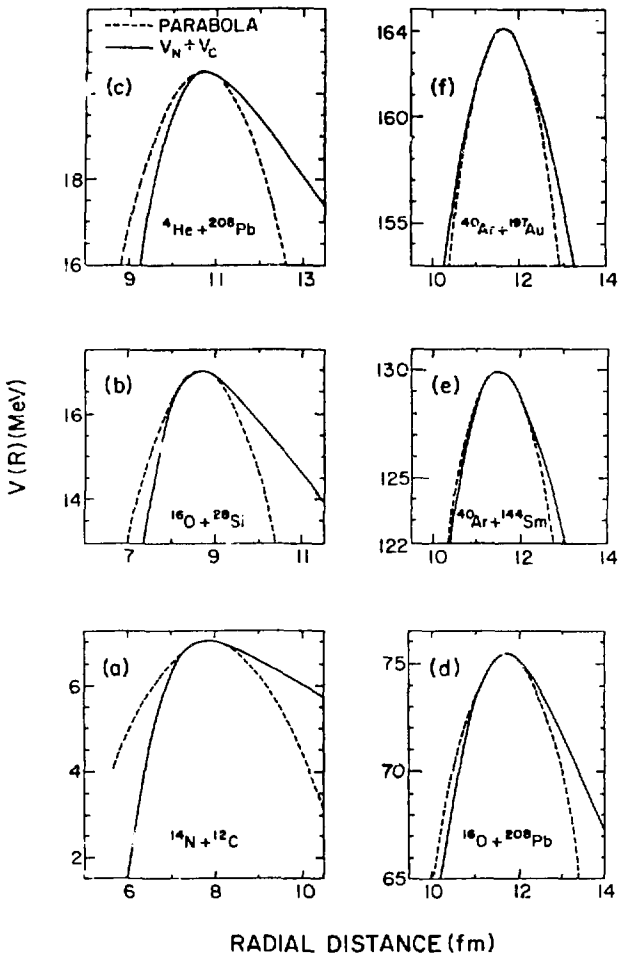


Fig. 4. Coulomb plus-nuclear potentials for $\ell = 0$ as given by a modified proximity formulation (solid lines) and the inverted-parabola approximation (dashed lines) for a variety of nuclear systems.[16] The approximation appears best for the heaviest systems, but in each case the parabolic barrier is of a smaller (or at most equal) width than the realistic barrier.

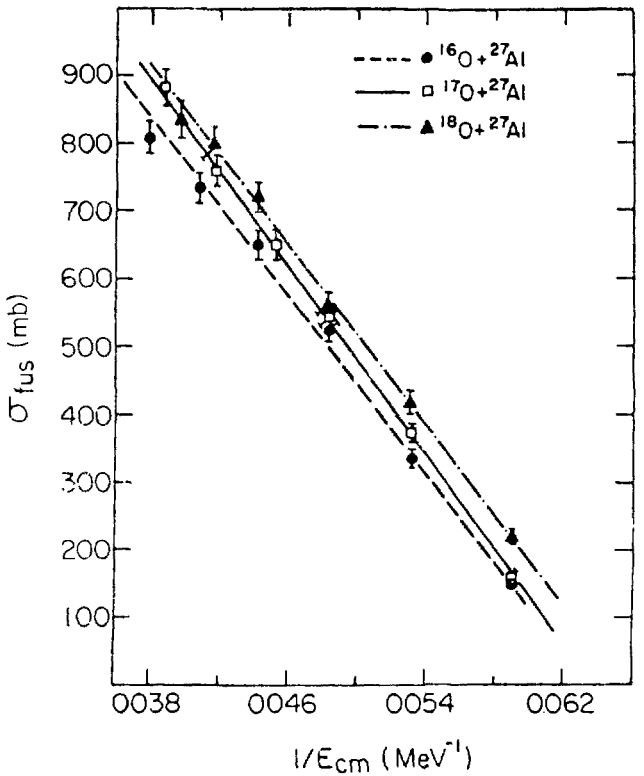


Fig. 5. Fusion cross sections for the systems $^{16,17,18}O + ^{27}Al$, measured in the energy region just above the S-wave barrier. In this region $\sigma_{fus}$ shows a classical 1/E behavior.

of the barrier as expressed by the oscillator energy $\hbar\omega_\ell$, and the moment of inertia in the centrifugal term, $2\mu r_{max}^2$.

In a classical approximation, $T_\ell$ is either zero or unity depending on whether $E_{c.m.}$ is less than or greater than $V_\ell(r_{max})$. In this case,

$$\sigma_{fus} = \pi r_{max}^2 \left| 1 - \frac{V(r_{max})}{E_{c.m.}} \right|$$

and only two parameters determine $\sigma_{fus}$. Figure 5 illustrates the application of this "$1/E_{c.m.}$" formula.[17]

The concepts of quantum mechanical barrier penetration at low energies, the classical "1/E" behavior at energies not too far above the barrier, and the requirement of penetration to a critical radius are combined in the five parameter formula of Glas and Mosel.[10] The inner critical radius $R_{cr}$ defines a critical angular momentum $\ell_c$, given by

$$\ell_c(\ell_c+1) = \frac{2\mu R_{cr}^2}{\hbar^2} \left( E_{c.m.} - V_{\ell=0}(R_{cr}) \right).$$

The height of the outer barrier is specified as usual by

$$V_{B\ell} = V_{\ell=0}(R_B) + \frac{\hbar^2 \ell(\ell+1)}{2\mu R_B^2}$$

and

$$\sigma_{fus} = \pi\lambda^2 \sum_{\ell=0}^{\ell_c} (2\ell+1) \left( 1 + \exp\left[ \frac{2\pi(V_{B\ell} - E_{c.m.})}{\hbar\omega} \right] \right)^{-1}.$$

Figure 6 illustrates the characteristic behavior of $\sigma_{fus}$ in the different energy regions.

$$\sigma_{fus} \longrightarrow \pi R_B^2 \left( 1 - \frac{V(R_B)}{E} \right), \text{ LOW ENERGIES}$$

$$\sigma_{fus} \longrightarrow \pi R_{cr}^2 \left( 1 - \frac{V(R_{cr})}{E} \right), \text{ HIGH ENERGIES}$$

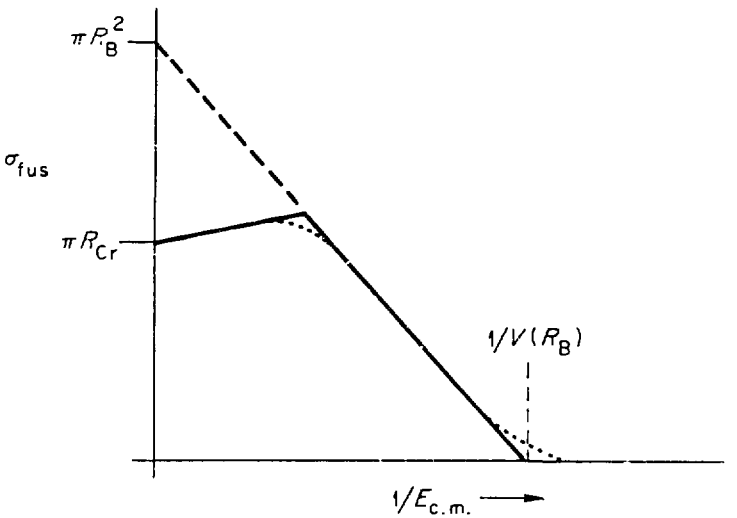


Fig. 6. Illustration of the parameter dependence of Glas' and Mosel's formula for the fusion cross section.[10] The dotted lines show the effect of the curvature of the potential in the respective barrier regions.

### F. Nuclear Structure and Microscopic Effects.

The foregoing discussion has delt briefly with some of the methods for describing the magnitude and energy dependence of fusion cross sections. Should it prove possible to describe the experimental data with the one-dimensional approximation, and with potentials, critical angular momenta and critical radii which vary smoothly from one nuclear system to the next, then our "zero order" description of fusion will contain all there is to know. The "nuclear structure" in fusion will consist of radii varying as $A^{1/3}$ and other characteristics of a liquid drop. However, this is not what we have in mind when we talk about nuclear structure or microscopic effects in fusion. Here we are referring to the deviations from the zero order predictions described above. (This is much the same as shell effects represent deviations from liquid drop binding energies.) Do the data show such nuclear structure effects? That is the subject of the next three sections.

## III. Subbarrier Fusion Cross Sections for Light Systems.

### A. Motivation

The motivation for measuring fusion cross sections for light systems such as $^{12}C + ^{12}C$ and $^{12}C + ^{16}O$ came first from the nuclear astrophysicists.[18] These reactions are of importance in the later stages of nucleosynthesis when a star has exhausted its hydrogen fuel to yield helium, and the triple alpha process ($\alpha + \alpha \rightarrow ^{8}Be$, $\alpha + ^{8}Be \rightarrow ^{12}C$) has produced a carbon core. The particular path that a star takes at this point is governed by its mass and the rate of the $^{12}C + ^{12}C$ reaction at $\approx 1$ MeV (c.m.)

Thus, the need to extrapolate this reaction cross section to low energies has resulted in much experimental work aimed at measuring small cross sections at the lowest possible energies.

The discovery of structure in the excitation function for $^{12}C + ^{12}C$ aroused interest in the reaction mechanism which continues unabated. (N. Cindro, this conference.) It thus became imperative to extend the measurements to other systems, even though they are not of equivalent astrophysical importance. Although a lot of work has been done in the 1970's, the fine art of measuring vanishingly small cross sections is still practiced at a number of laboratories.[18]

Another reason for studying reactions at sub-Coulomb energies is the high sensitivity of the cross section to small changes in the potential. This sensitivity is explained in Eq. 3 where the integral of the wave number over the classically forbidden region appears in the argument of an exponential. The exploitation of this sensitivity requires the measurement of small cross sections with high precision, a fact which bears directly on the choice of the experimental method.

## B. Experimental Method

The formation and decay of a compound nucleus may be detected in several ways. Since fission is not a significant decay mode for the light nuclei considered here, one may observe either the promptly evaporated particles (protons, neutrons, alpha particles), or detect the residual heavy nucleus via its prompt gamma-ray emission or a delayed activity. Small cross sections require both high efficiency and high selectivity in distinguishing background radiation originating

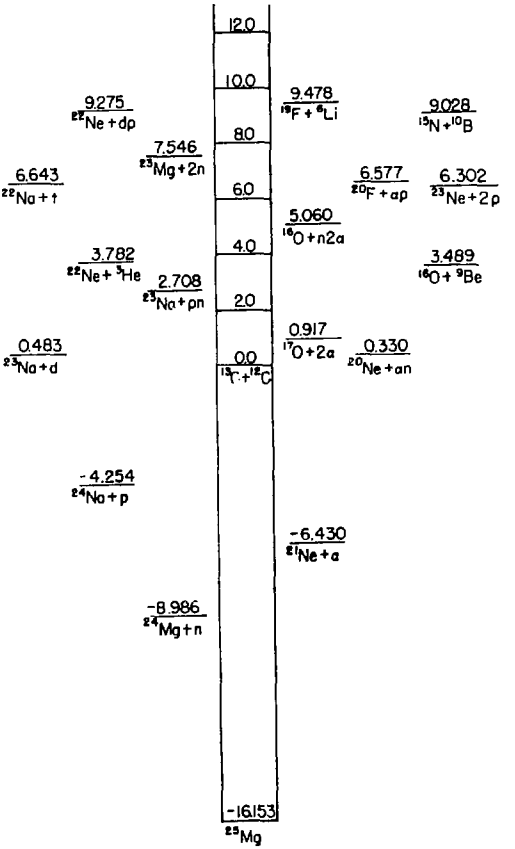


Fig. 7. Thresholds for decay of $^{25}Mg$ relative to the separation energy for $^{13}C + ^{12}C$. The locations of bombarding energies of 2,4,6, MeV (c.m.) are indicated.

with contaminants in the target. The Ge(Li) detector provides a very effective compromise between these two usually conflicting requirements. It has the great advantage that γ-rays produced by contaminants are usually resolved from the transition of interest. This type of detector is used frequently in such studies, and we will illustrate its operation with the $^{12}C + ^{13}C$ reaction.[19]

In general, the γ-ray spectra taken with a Ge(Li) detector for low energy heavy-ion reactions reveal the lowest-lying transitions in the heavy residual nuclei produced by p-, n-, and α-emission from the compound system. Depending on the particular Q-values, one also observes transitions for successive pn, nα and pα emission as the bombarding energy is increased. Figure 7 shows the relevant thresholds for $^{12}C + ^{13}C$ induced reactions. Because of the generally positive Q-values, a change of several MeV excitation in the compound nucleus will not have a great effect on its average decay into different channels. At the least, these changes will be small compared with the order-of-magnitude changes occurring in the cross section for formation of the compound nucleus because of the Coulomb barrier in the entrance channel. This is the crucial element which allows one to obtain total cross sections from measurements of γ-ray yields for individual transitions in the heavy residual nuclei.

A typical γ-ray spectrum is shown in Fig. 8. Prominent γ-ray lines are labeled by the evaporated light particle or particles associated with the residual nucleus having that γ-ray transition. The absolute cross sections for the production of individual evaporation residues (e.g. $^{24}Mg$ or $^{21}Ne$) can be deduced through statistical model estimates

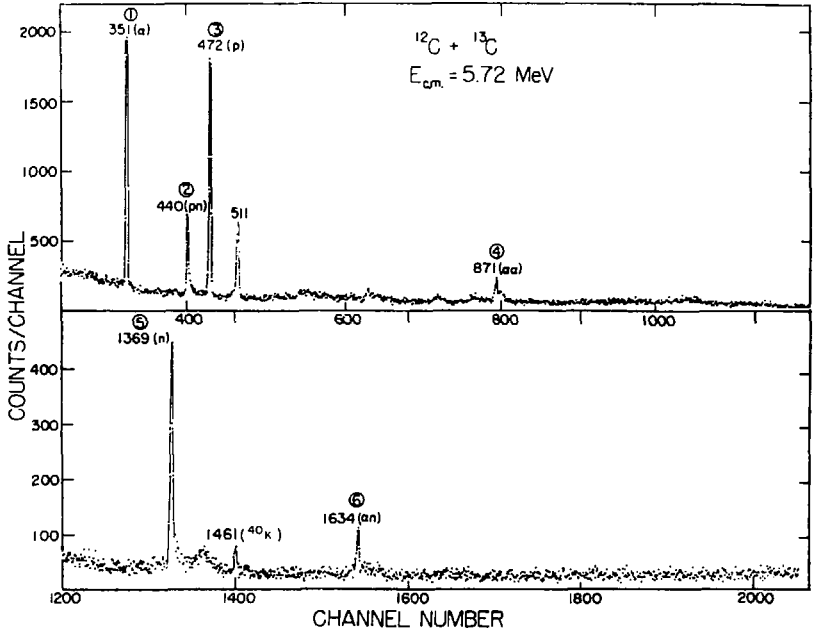


Fig. 8. A typical γ-ray spectrum obtained with a $^{12}C$ beam and a carbon target enriched to 90% in $^{13}C$. The origins of the prominent transitions are indicated by the associated light particles evaporated from the compound nucleus.

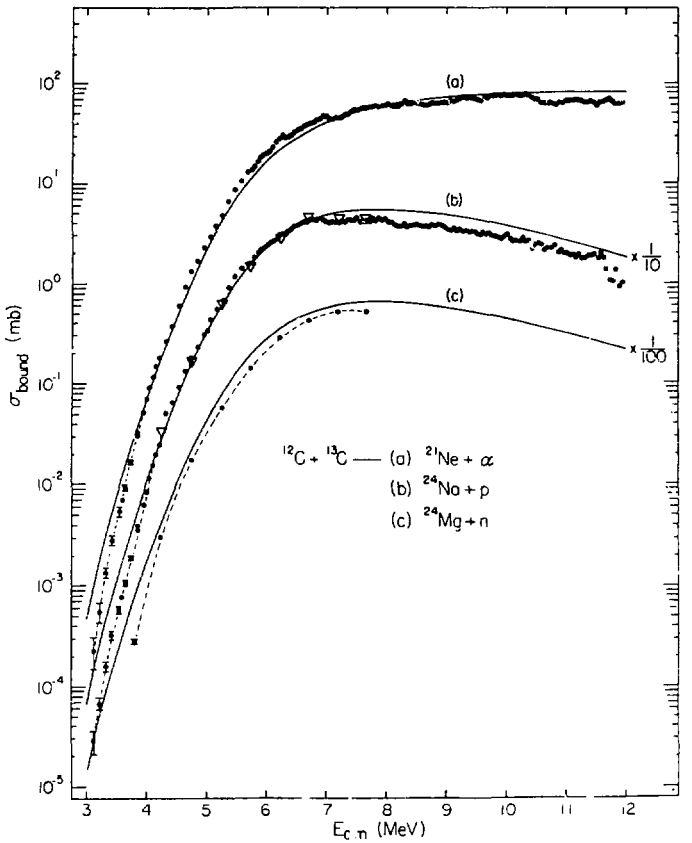


Fig. 9. Cross sections for the primary emission of $\alpha$-particles, protons and neutrons populating particle-bound states in the corresponding residual nuclei. The open triangles correspond to measurements of the delayed $^{24}Na$ activity. The full curves are the results of Hauser-Feshbach calculations. The predicted relative yields Ne, Na, and Mg are not very sensitive to the choice of potential parameters for the entrance channel.

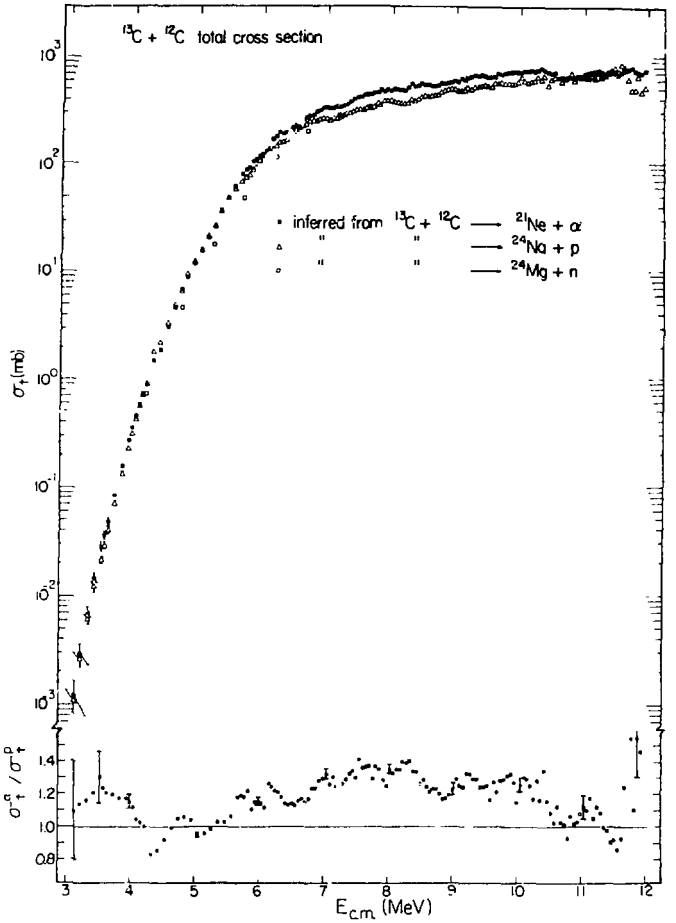


Fig. 10. The cross section for compound nucleus formation inferred independently from the experimental yields for the lowest γ-ray transitions in $^{21}Ne$, $^{24}Na$, and $^{24}Mg$. The lower part of the figure shows the ratio of α-emission to proton emission.

of the relative populations of the levels in the residual nucleus, and the known branching ratios of the low lying levels. Figure 9 shows the cross sections so deduced for populating bound levels of $^{21}$Ne, $^{24}$Na and $^{24}$Mg. Note that the population of $^{24}$Na (curve b) could be determined in two ways--by the prompt 0.472 MeV γ-ray in $^{24}$Na (solid points) and by the delayed decay of $^{24}$Na → $^{24}$Mg, measured out of beam (open triangles). The two methods are in good agreement.

The desired quantity, of course, is the total fusion cross section, and this may be obtained from the data in Fig. 9 by applying a correction for that fraction of compound nuclei which do not produce a particle-bound nucleus of $^{21}$Ne, $^{24}$Na or $^{24}$Mg. This correction is calculated with the statistical model. The predictions of the statistical model for the yields to the bound states themselves are compared with the data in Fig. 9. The important point to note is that the correction factors change rather slowly with bombarding energy, whereas the cross section itself changes 5 orders of magnitude in 3 MeV. The total fusion cross section is shown in Fig. 10. The cross section at energies above 7 MeV is in the classical region (i.e. linear with 1/E), while the subbarrier region and exponential variation of $\sigma_{fus}$ is at the lower bombarding energies.

## C. Systematics

### 1. *The Standard Prediction*

These measurements of the $^{12}$C + $^{13}$C fusion reaction illustrate one of the main experimental techniques for determining fusion cross sections, and give us a familiarity with the type of results which can be obtained. Now we want to return to the question of nuclear structure effects, bearing in mind our definition at the end of Section II. To do this, we

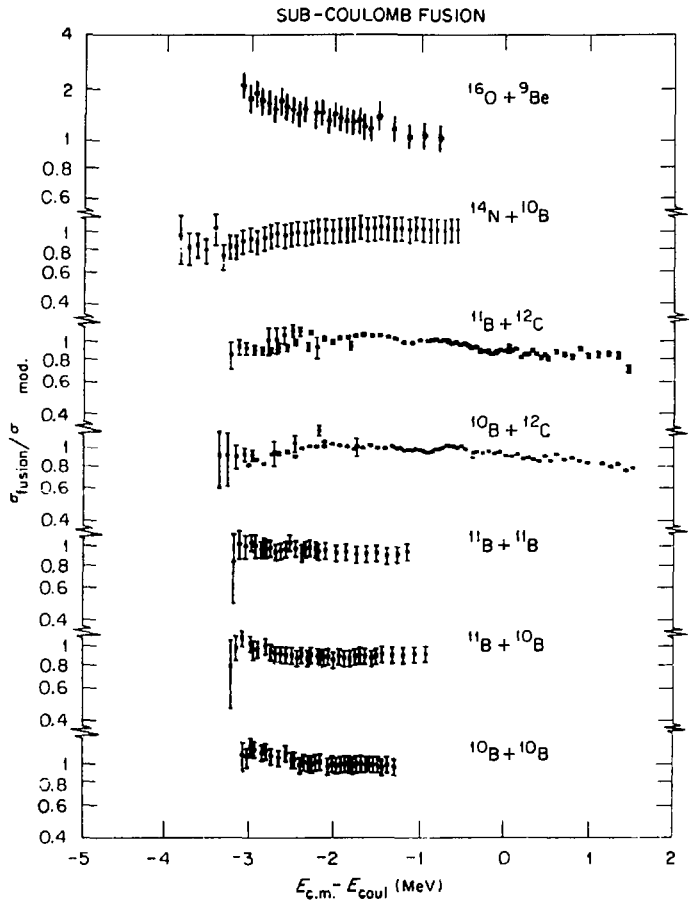


Fig. 11. The ratio of measured fusion cross sections to a standard prediction for sub-Coulomb energies. The energy scale in each case has been shifted such that 0-MeV corresponds to $E_{c.m.} = Z_1 Z_2 e^2/R$ MeV where $R = 1.7\ (A_1^{1/3} + A^{1/3})$. The experimental data are taken from $^{10}B + ^{10}B$, $^{11}B + ^{10}B$, $^{11}B + ^{11}B$ (Ref. 20); $^{10}B + ^{12}C$, $^{11}B + ^{12}C$ (Refs. 21,22); $^{14}N + ^{10}B$ (Ref. 22); and $^{16}O + ^{9}Be$ (Ref. 23). See also Ref. 24.

have to factor out the "zero-order" dependence of $\sigma_{fus}$ on the bombarding energy, and look at the sysematics for a large number of reactions.

There are many ways in which one can eliminate the gross exponential dependence of $\sigma_{fus}$ on bombarding energy. It does not matter too much which method one chooses, so long as one is consistent in the treatment of the different systems. In our case we will make a standard prediction based on a complex potential (V = 50 MeV, W = 10 MeV, $r_o$ = 1.27 and a = 0.4 fm) in which we have taken care that the imaginary potential is sufficiently strong to prevent resonances in the pocket of the potential (see Fig. 2). We divide each cross section by the $\sigma_{mod}$ given by the solution of the Schrödinger equation. This reduces the energy dependence from five orders of magnitude to at most one order of magnitude. Since the barriers for the different systems occur at different energies because of differences in the Coulomb barrier, we shift each energy scale by an amount $E_{Coul} = Z_1 Z_2 e^2/R$ where $R = 1.7\ (A_1^{1/3} + A_2^{1/3})$.

The ratio $R = \sigma_{fus}/\sigma_{mod}$ for a number of systems[20-24] involving the fusion of boron isotopes is shown in Fig. 11. The ratios are near unity and the standard, or zero order, calculation thus reproduces these data rather well. Given our operational definition of nuclear structure effects, we would not cite any evidence for microscopic effects based on a comparison of the lower six excitation functions shown in Fig. 11.

2. Neutron Transfer

The energy dependence for $^{16}O + {}^{9}Be$,[23] however, is quite different from that of the boron isotopes, with R rising by a factor of 2 from the highest to the lowest bombarding energy. Although not shown in this figure, $\sigma_{fus}$ for $^{12}C + {}^{9}Be$ has a very similar behavior.[23,25]

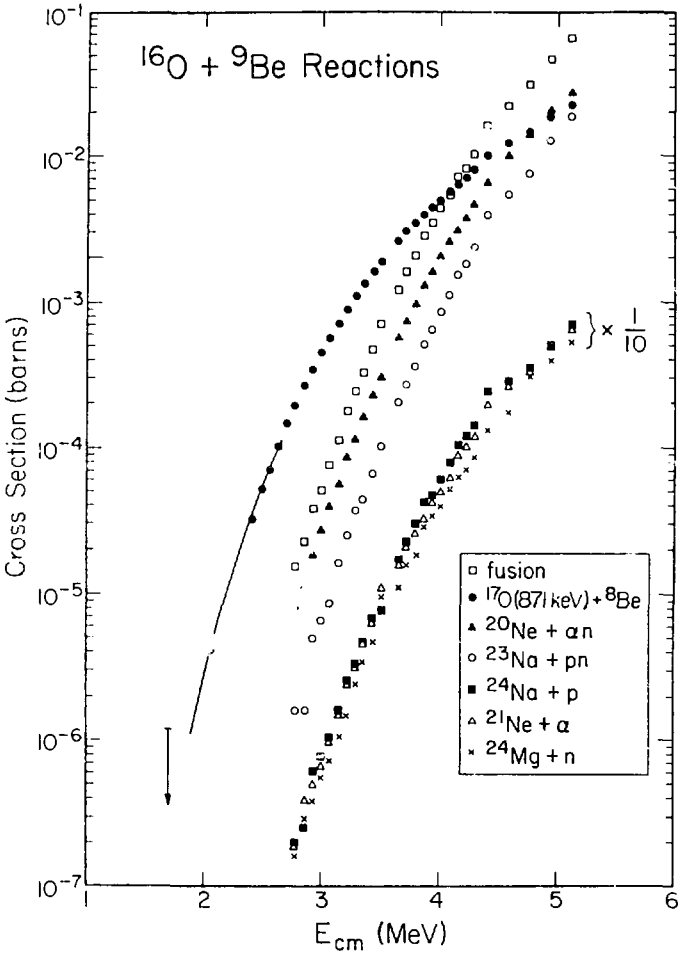


Fig. 12. $^{16}O + {}^{9}Be$ partial reaction cross sections. The open squares, representing the total fusion yield, were obtained by summing the partial cross sections excluding $^{17}O^{*} + {}^{8}Be$. The neutron transfer cross section (solid data) exceeds $\sigma_{fus}$ at energies below 4 MeV c.m. (Ref. 23).

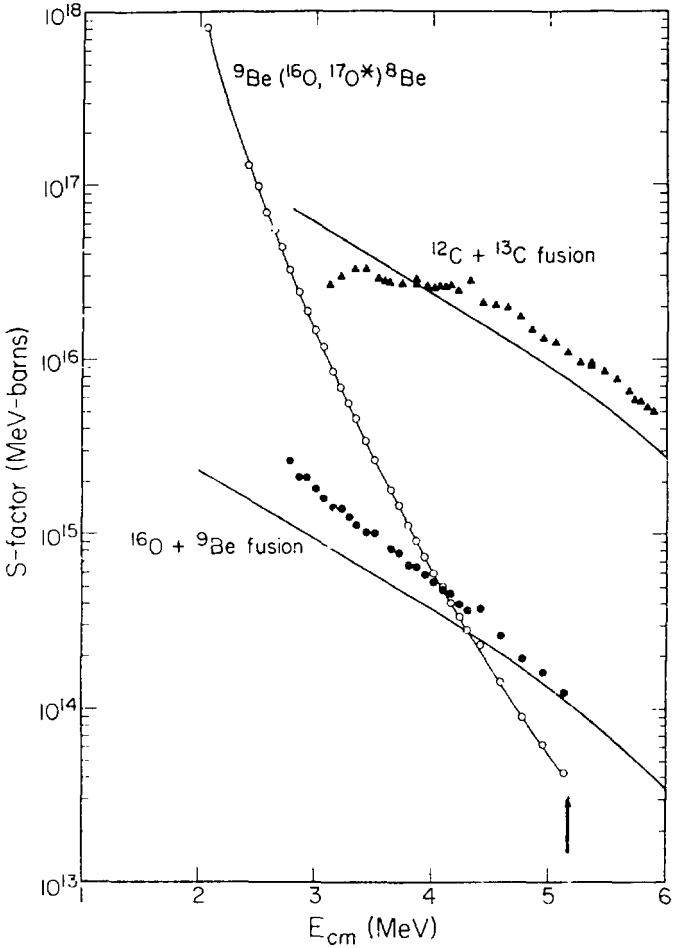


Fig. 13. Nuclear reaction S-factors for formation of $^{25}$Mg via the reactions $^{16}$O + $^{9}$Be (Ref. 23) and $^{12}$C + $^{13}$C, (Ref. 19). The S-factor for the neutron transfer reaction $^{16}$O + $^{9}$Be → $^{17}$O* (.87 MeV) + $^{8}$Be is shown for reference. The arrow indicates the height of the interaction barrier. The full curves are calculations of $\sigma_{fus}$ using the standard complex potential described in the text. (from Ref. 23).

Now these reactions have in common the interesting feature that the kinematic conditions for neutron transfer in the reactions $^{9}Be(^{16}O, ^{17}O^{*})$ and $^{9}Be(^{12}C, ^{13}C^{*})$ are optimum[26] and indeed these reactions have larger cross sections at the lower bombarding energies than does fusion. This is illustrated in Fig. 12 for the case[23] of $^{16}O + ^{9}Be$. Below 4 MeV c.m., the cross section for neutron transfer to the $1/2^{+}$, 0.871 MeV state in $^{17}O$ increasingly dominates the fusion cross section.

It is therefore tempting to speculate that the availability of a loosely bound valence neutron whose (inelastic) transfer is kinematically favored may be influencing the cross section for fusion. This would be an excellent example of a nuclear structure effect on fusion. There are two other systems for which a single neutron transfer is favored, $^{10}B + ^{11}B$ and $^{12}C + ^{13}C$. In these cases it is the transfer to the ground state, i.e. elastic transfer, which has the optimum Q-value. Figure 11 shows that $^{11}B + ^{10}B$ does not indicate any enhancement of the fusion cross section at low energies. Figure 13 compares the energy dependence of $^{16}O + ^{9}Be$ and $^{12}C + ^{13}C$. The format of the comparison in this case happens to be in terms of the nuclear reaction S-factor[+] defined by $S = \sigma_{fus} E \cdot \exp 2\pi\eta$ where $\eta = Z_1 Z_2 e^2/\hbar v$. Again, the reaction involving elastic neutron transfer, $^{12}C + ^{13}C$, does not show a relative up-turn at low energies. Thus, if our speculation is correct that a propensity for neutron transfer influences the energy dependence of the fusion cross section, then it appears that only inelastic processes (and not elastic transfer) are effective. The speculative nature of these remarks need hardly be

[+]The S-wave Coulomb penetration factor $\propto \exp 2\pi\eta$, does not reproduce very well the energy dependence of heavy ion fusion reactions. Its only advantage in comparing different reactions is that it contains no ajustable parameters.

underlined; theoretical calculations could contribute to a more quantative discussion of these possibilities.

## 3. Energy-averaged Structure

The values of $R = \sigma_{fus}/\sigma_{mod}$ for systems involving projectiles and targets both with masses $\geq 12$ are shown in Fig. 14. The difference between the smooth curves in Fig. 11 and the structure shown in Fig. 14 is striking. (The narrow resonances in $^{12}C + ^{12}C$ and to a lesser extent in $^{16}O + ^{12}C$ are noteworthy, but that is in Dr. Cindro's domain; we are concerned here with the energy-averaged behavior of the data.) A general feature for the systems in Fig. 14 is that R decreases at lower energies. (Recent measurements by Ketner et. al.[28] do not confirm the upward trend in $^{12}C + ^{12}C$ at the lowest energies observed by Mazarakis and Stephens and shown in Fig. 14.) Apart from this similarity, the behavior of the individual systems shown in Fig. 14 is varied. For example, the average energy dependence of R for $^{16}O + ^{14}N$ is quite different from that of $^{16}O + ^{16}O$. The systems $^{14}N + ^{12}C$, $^{13}C + ^{12}C$ and $^{12}C + ^{12}C$ are all different and the differences can be quite large, up to factors of two.

Figures 11-14 also contain a number of cases in which the same compound system (i.e. same charge and mass) is reached via two different entrance channels. These cases are: $^{21}Ne$($^{12}C + ^{9}Be$, $^{11}B + ^{10}B$); $^{24}Mg$($^{14}N + ^{10}B$, $^{12}C + ^{12}C$); $^{25}Mg$($^{16}O + ^{9}Be$, $^{12}C + ^{13}C$); $^{28}Si$($^{16}O + ^{12}C$, $^{14}N + ^{14}N$). Only in the last case does there appear to be a similarity: if the structure in $^{16}O + ^{12}C$ is averaged, its overall behaviour is similar to that of $^{14}N + ^{14}N$.

Note added in proof: See M. L. Chatterjee, L. Potvin and B. Cujec, Nucl. Phys. A333, 273 (1980) for a comparison of $^{12}C+^{12}C$, $^{12}C+^{13}C$, and $^{13}C+^{13}C$.

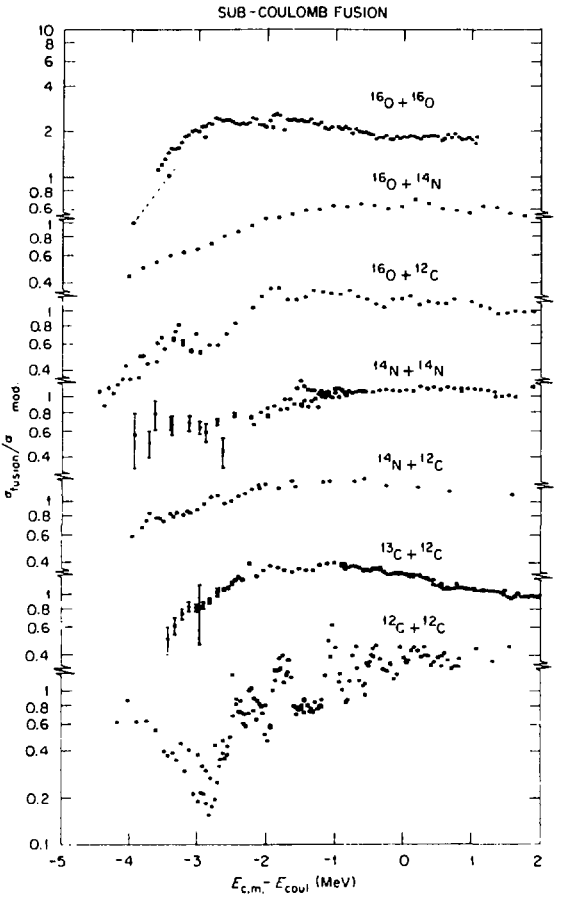


Fig. 14. See the caption to Fig. 11. The experimental data are taken from $^{12}C + ^{12}C$ (Ref. 27), $^{12}C + ^{13}C$ (Ref. 19), $^{14}N + ^{12}C$, $^{16}O$ (Ref. 29), $^{12}C + ^{16}O$ (Ref. 30), $^{14}N + ^{14}N$ (Ref. 31) $^{16}O + ^{16}O$ (Ref. 32). See also Ref. 24.

Recently, measurements of $\sigma_{fus}$ for $^{16}O + {}^{16}O$ and $^{12}C + {}^{20}Ne$ have been made by Hulke et. al.[33], permitting a comparison of two reactions which produce the same compound system at similar excitation energies ($\Delta Q \sim 2.4$ MeV). These results, shown in Fig. 15a have a number of interesting features. First at energies well above the barrier, $\sigma_{fus}$ ($^{16}O + {}^{16}O$) $\approx 2 \times \sigma_{fus}$ ($^{12}C + {}^{20}Ne$). Hulke et. al.[33] confirm the measurements of Spinka and Winkler[32] for $^{16}O + {}^{16}O$, thus apparently setting this system apart from all others in Figs. 11 and 14 as one for which $\sigma_{fus}/\sigma_{mod} \rightarrow 2$ at above the barrier (!) whereas all other systems have $\sigma_{fus}/\sigma_{mod} \rightarrow 1$. This appears remarkable in that the region just above the barrier is otherwise much less sensitive to structure effects.[34]

There are several experiments, however, using charged particle detection of the residues which are in disagreement with the results obtained by the $\gamma$ ray method. The discrepancy is about a factor of two. The different results are summarised in Table I (from Ref. 33). It is particularly distrubing that the larger value of the cross section is inconsistent with an analysis of the elastic scattering.[7] Before citing $^{16}O + {}^{16}O$ as the exception to the rule, $\sigma_{fus}/\sigma_{mod} \rightarrow 1$ for $E \gtrsim E_B$, the experimental discrepancy in the absolute noramalizations for this particular case will have to be removed.

The relative energy dependence of the two systems is less dependent on the overall normalization and these are seen to be different. At energies below the barrier, $\sigma_{fus}$ (C + Ne) $> \sigma_{fus}$ (O + O) at the same center of mass energy as expected because of the lower Coulomb barrier for C + Ne. However, if a simple energy shift for the difference in Coulomb barriers is made, the O + O cross section exceeds that for Ne + C. This is true even when the shift in Coulomb barriers is minimized by taking a radius parameter $r_o = 1.9$ fm. (Fig. 15b). This excess fusion cross section for O + O (after a correction for the Coulomb

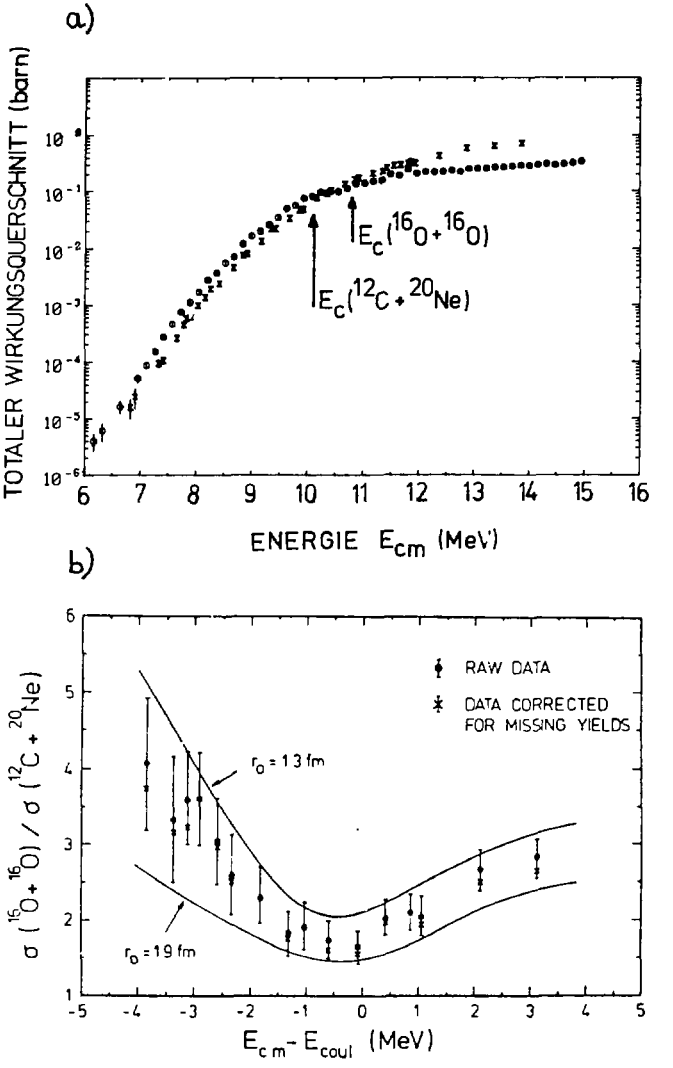


Fig. 15 (a) Fusion cross sections for $^{16}O + ^{16}O$ (crosses) and $^{12}C + ^{20}Ne$ (circles) from Ref. 33.
(b) The ratio of the cross-sections plotted against the energy above the barrier ($r_o$ = 1.7 fm). The range of results obtained for barriers calculated with radius parameters between 1.3 and 1.9 fm is indicated by the full curves.

Table I.

Comparison of experimental total fusion cross sections for the $^{16}O + {}^{16}O$ reaction. (From Hulke et. al. 33).

| Reference | Detection Method | $E_{c.m.}$ (MeV) | $\sigma_{fus}$(mb) | $\sigma_{fus}$(mb at $E_{c.m.}$ = 11.85 MeV[a]) |
|---|---|---|---|---|
| Apinka+Winkler [30] | light particles[b] | 11.85 | 400±100[c] | 400[c] |
| Tserruya et.al. [31] | heavy residues | 13.50 | 410±40 | 205 |
| Kovar et.al. [32] | heavy residues | 14.92 | 435±30 | 145 |
| Kolata et.al. [36] | γ-rays | 12.28 | 270±20[d] | 210[d] |
| Chene et.al. [37] | γ-rays | 12.25 | 200±15[d] | 155[d] |
| Wu+Barnes [38] | γ-rays | 12.00 | 438±66 | 390 |
| Hulke et.al. [33] | γ-rays | 11.85 | 450±100 | 450 |

[a] Extrapolated values from the observed (γ-ray) energy dependence of $\sigma_{fus}$

[b] Other techniques also used.

[c] Lower limit is 328 mb, upper limit is 476 mb; the average value is given.

[d] Lower limit, since no corrections were applied for missing yields and summing effects.

barrier is made) is also in a direction opposite to that expected on the basis of the deformed nature of $^{12}C$ and $^{20}Ne$ and spherical character of $^{16}O$. (This point will be discussed in Section V).

The message of Figs. 11-14 is clear. The addition or removal of one or two nucleons from the projectile or target can have a profound effect upon the energy dependence for fusion. This is a strong indication that the valence nucleons play an important role in the mechanisms leading to fusion, i.e. that nuclear structure is affecting the fusion process.

## D. Theoretical Approaches.

### 1. The Entrance Channel

There is at present no theoretical explanation for the different behavior shown by these systems. Several ways in which nuclear structure enters into the detemination of nuclear potentials have been mentioned in the previous section, however, and it is useful to speculate on the types of calculation which might yield an explanation.

A first avenue to explore is the effect of valence nucleons on the nucleus-nucleus real potential. One way this can be done is in the context of a folding model.[1] This model makes the assumption that the nuclear densities are frozen during the interaction, an assumption which is better at higher bombarding energies. Nevertheless, it is of interest to see what happens when the contributions of individual nucleons to the overall potential are estimated. This has been done by Wieland and Satchler,[39] who used, in addition to the folded potential, the same imaginary potential as in the standard model calculations (i.e. $W = 10$ MeV, $r_I = 1.27$, $a_I = 0.4$). The results of these calculations were nearly indistinguishable from standard calculations. Other ways in which the shell structure of nuclei can be incorporated in the real interaction

potential are the TDHF approximation[4,40] and the two-center shell model.[2] In view of the results obtained with the folding model and with the TDHF (Ref. 40), however, a microscopic explanation of the data would seem to require a consideration of nuclear structure effects on the imaginary potential.

In the two center shell model, inelastic processes can occur at internuclear separations where the levels of the system cross. The two center shell model levels for the reactions $^{12}C + {}^{17}O$ and $^{13}C + {}^{16}O$, calculated by Park et. al.,[41] are shown in Fig. 16. In this case one can see that the probability for a neutron transfer (at either a real or an avoided level crossing), will be different for each of these systems. (In one case the loosely bound neutron is in the $p_{1/2}$ shell, in the other case, in the $d_{5/2}$ shell.) The likelihood of an inelastic process as the nuclei approach could naturally influence the probability for fusion, since the latter can be viewed as the culmination of many successive inelastic processes. (In this context, the speculations made earlier on the $^{16}O + {}^{9}Be$ and $^{12}C + {}^{9}Be$ fusion reactions seem plausible.) What is needed, of course, are calculations in which the dynamical aspects of the reaction are included.

The methods of calculating the imaginary potenial within the context of the two center shell model should be mentioned at this point. The first is the use of the Landau-Zener approximation by Glas and Mosel to estimate the probability of inelastic processes at level crossings,[3] and the level-density approach of von Charzewski et. al.[42] In these cases the two center shell model enters through the specification of the location of the level crossings and the number of accessible 1 particle-1 hole states (i.e. precompound states), respectively.

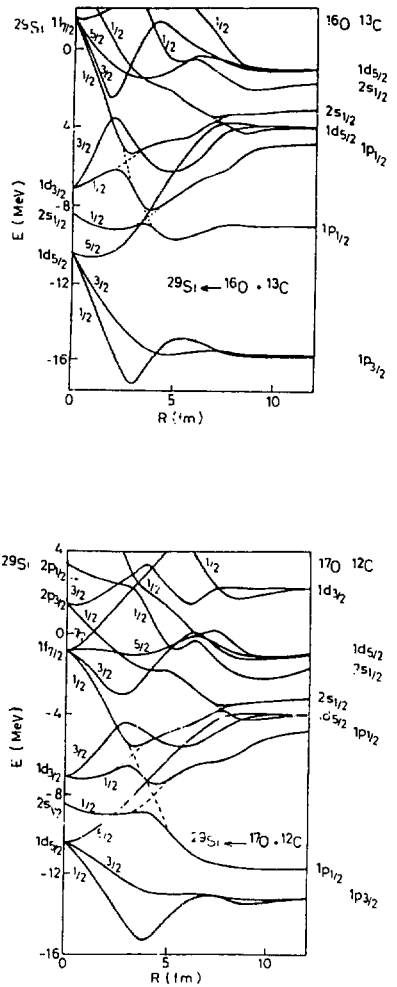


Fig. 16. Two center shell model calculations of the neutron levels for two different entrance channels populating the same compound nucleus, $^{29}$Si. (Ref. 41). The dashed lines indicate avoided level crossings.

## 2. The Compound Nucleus

The compound nuclei formed in the above reactions are generally at excitation energies greater than 15 MeV and, because of the low bombarding energies, have angular momenta well above the yrast line. The densities of levels or number of channels open for decay are thus large. Nevertheless, some systems will have, because of differences in Q-value, densities of levels much higher than others. Systems with larger Q-values and this high densities of levels have a tendency to exhibit smooth fusion excitation functions, devoid of intermediate structure resonances.[43] A classic example is given by the $^{14}N + ^{10}B$ and $^{12}C + ^{12}C$ systems ($\Delta Q \sim 10$ MeV).

Beyond the question of intermediate structure, its presence and absense, there does not appear to be any noticeable correlation between the energy-averaged behavior of the systems shown in Figs. 11 and 14 with the number of open channels for decay of the compound nucleus given in Table I of Ref. 43.

The best prospects for understanding the nuclear structure effects in the experimental data for light systems at subbarrier energies appear to lie with the role which valence nucleons play in various inelastic processes in the entrance channel. Progress over the years has been slow, but the outlook is encouraging.

## IV. The Fusion of Light Systems at High Energies

### A. Motivation

The pronounced differences in the energy dependence of $\sigma_{fus}$ at sub-barrier energies seem to disappear above the barrier. Thus, with the possible exception of $^{16}O + {}^{16}O$, all of the systems examined in Section III followed the standard prediction in the energy region where $\sigma_{fus} \propto \pi R^2(1-V/E)$ (see Fig. 5). A systematic study[34] of many systems in this energy region indicates that the parameters R and V vary rather smoothly from one system to the next. This fact by itself offers little motivation to extend measurements of $\sigma_{fus}$ to even higher energies, at least from the point of view of nuclear structure effects. Fortunately there were a number of other reasons for pushing to higher energies. These included the study of the compound nucleus at high excitation and high angular momentum, the question of the liquid drop limit,[44] and the competition between fusion and direct reaction channels. The measurements revealed the unexpected, of course, and marked differences were found in the behaviour of systems varying by only a few nucleons. Energy-averaged structure, often referred to as oscillations and reminiscent of that seen in $^{12}C + {}^{12}C$ and $^{12}C + {}^{16}O$, was found to persist in these systems at energies where reaction channels other than fusion begin to complete. In most other systems this structure is absent or much attenuated. The maximum fusion cross section, defined simply as the largest value of $\sigma_{fus}$ measured at any bombarding energy, was seen to vary by several hundred millibarns from system to system.[34,45,46] The studies referred to here[34,45,46] have been made with tandem Van de Graff accelerators and, therefore, are limited to the energy

region above the barrier where direct reactions first become significant. Beyond this lies a vast energy region in which the collision becomes progressively more violent. Cyclotrons are needed to provide the required bombarding energies, and finely stepped excitation functions are replaced by measurement intervals of twenty to fifty MeV. It is on this type of study that I want to concentrate. As might be expected, the experimental methods and the problems encountered in analysing the data are quite different from those of the subbarrier region.

## B. Experimental Method

At high bombarding energies the evaporation residues have a kinetic energy sufficient to permit their Z-identification by the standard ΔE-E telescope. In our work[47-50] (most of which has been done at ORNL) we have used a gas ionization chamber in conjunction with a position sensitive solid state detector.[51] This system, which can also be used with a gas cell target,[52] enables the rapid acquisition of data simultaneously over an angular range of 9 degrees.

In contrast to measurements at low energies or with heavier targets, the evaporation residue cannot be identified on the basis of its mass or charge alone. Figure 17, which shows a two dimensional ΔE-E spectrum, illustrates this for the highest bombarding energy used, the 248 MeV $^{14}N$ beam from the LBL 88-inch cyclotron. A continuous distribution of reaction products from α-particles through neon is observed. Even though the compound nucleus is aluminum, the products Na and Mg are absent. This is a simple consequence of the high excitation energy (≈ 130 MeV) and angular momentum ( 26ħ) which must be dissipated by the rather light (A = 26) compound nucleus.

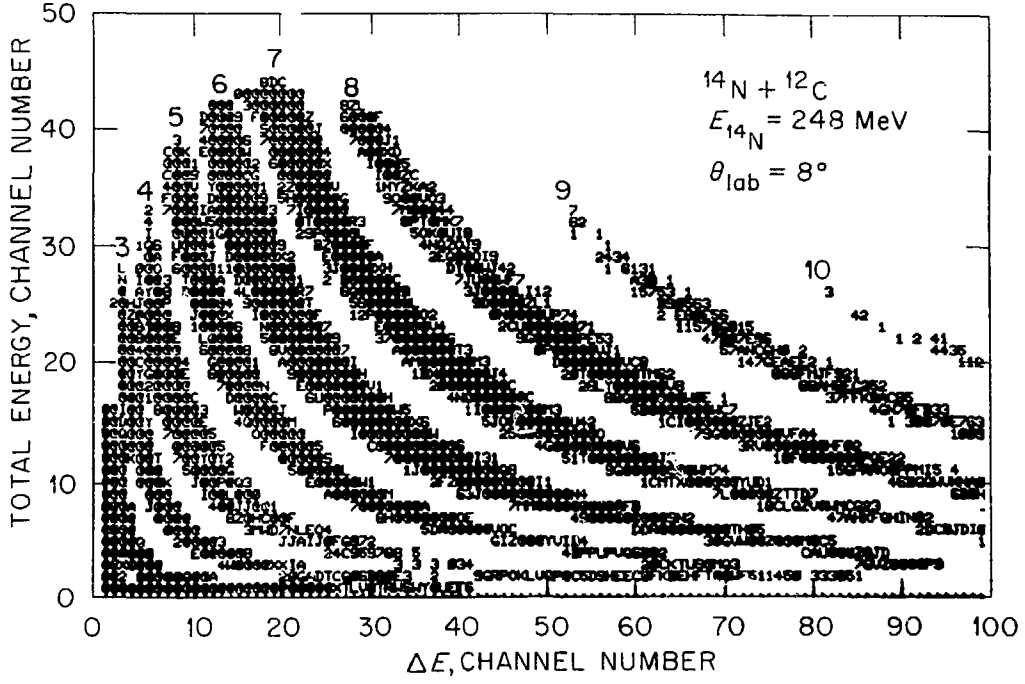


Fig. 17. A two dimensional ΔE-E spectrum of reaction products obtained at high energy. The Z of the products is indicated.

The average kinetic energies of an evaporation residue with Z = 7 and of an inelastically scattered nitrogen ion are quite different, however, as shown in Fig. 18. Thus, the kinematics of full momentum transfer associated with formation of a compound nucleus enable the separation of evaporation residues from products of peripheral collisions. That this is indeed the case has been demonstrated in detail in Ref. 49. The following discussion associated with Figs. 18-23 provides a brief illustration of the characteristic features of the data and the method for deducing $\sigma_{fus}$.

Providing the compound nucleus attains thermal equilibrium, its decay can be predicted with the statistical model. The combination of the Hauser-Feshbach formula with multi-step evaporation and a center-of-mass to laboratory transformation is accomplished by Monte Carlo techniques. The predictions of the energy-, and angle-, and Z-distributions of the residues shown in Figs. 18 and 20-24 have been made with the Code LILITA.[55] The generally good agreement between these predictions and the experimental data shows that the residues are properly identified and suggests that the compound nucleus attains equilibrium.

Figure 19 (a, bottom) displays a singles spectrum of carbon ions observed at $\theta_{lab} = 8^{o}$ for a beam energy of 185 MeV. The unfolding of the two components of the spectrum is indicated. Peripheral reactions should produce two fragments (plus perhaps an $\alpha$-particle or proton) whereas compound nucleus formation should produce only one fragment (the evaporation residue) which is in coincidence with many $\alpha$-particles, protons and neutrons. Figure 19b shows the spectrum of carbon ions in coincidence with other fragments of Z = 5, 6, and 7. The evaporation residue portion is absent. If a coincidence

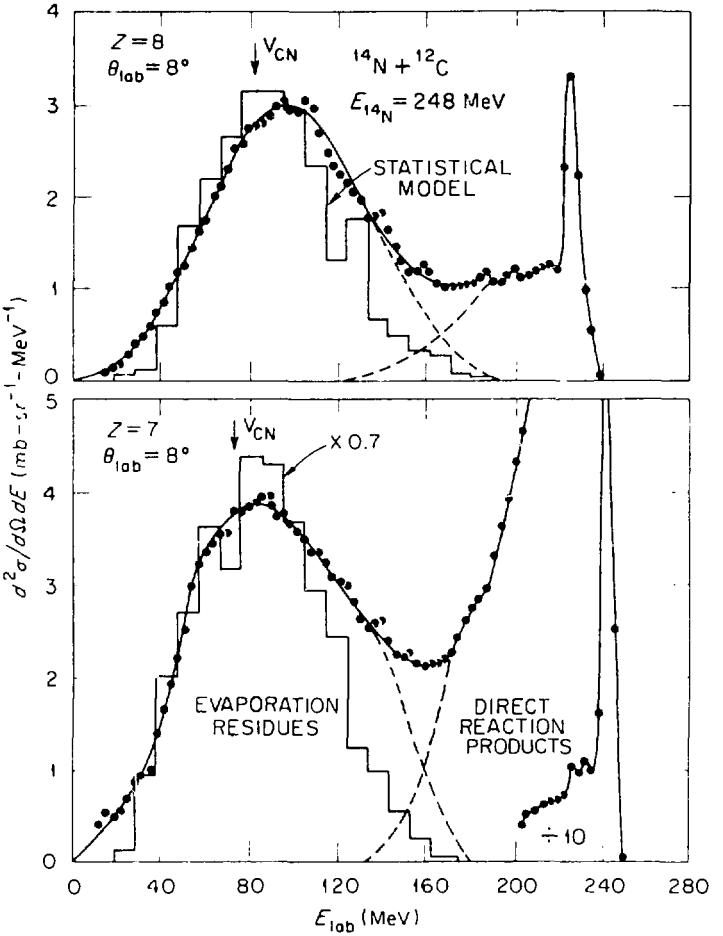


Fig. 18. Projections of data shown in Fig. 17 onto the energy axis. The unfolding of the spectra into direct and compound components is indicated.

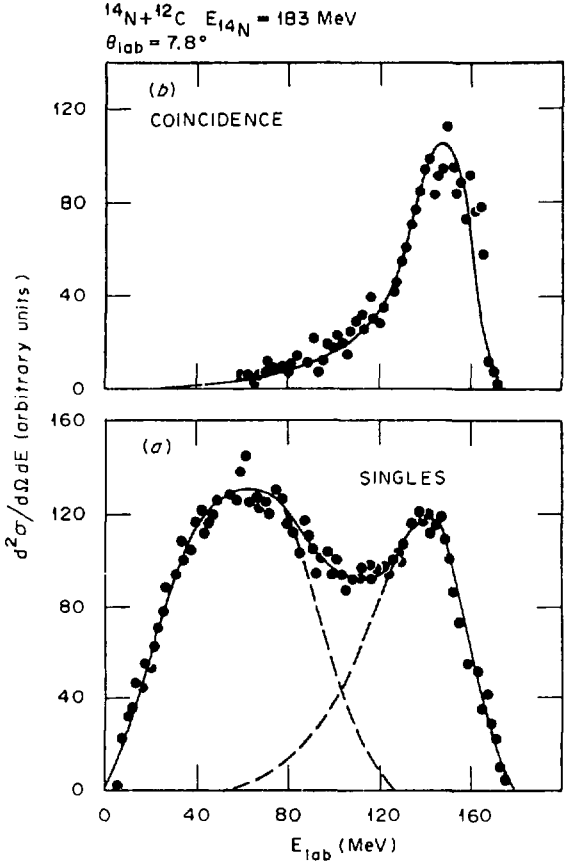


Fig. 19. Spectra of carbon ions in singles (bottom) and in coincidence (top) with ions of Z = 5, 6, and 7.

with α-particles (not shown) is required, the residue portion is enhanced relative to the direct reaction portion. While these observations are consistent with our expectations for compound and peripheral reactions, a more stringent test is made by observing the angular correlations of α-particles in coincidence with the residues. Figure 20 shows a comparison of such data and the Monte Carlo prediction (histogram). More extensive coincidence measurements, in which the energy spectra of α-particles at very forward angles will be studied, are in progress [54] These should provide confirmation of the conclusion drawn from the analysis of the singles spectra, viz., that the residues are the result of the complete amalgamation of the projectile with the target.

The angular distributions of evaporation residues and direct reaction products are compared in Fig. 21. The former are broad because of the recoil imparted through the evaporation of typically two alpha particles The latter exhibit the sharp forward peaking consistent with diffractive scattering at energies well above the Coulomb barrier. The slope of the diffraction model prediction is based on a fit to the elastic scattering. The statistical model reproduces the angular distribution of residues quite well.

The Z-distribution of evaporation residue products is obtained by integrating the respective angular distributions. A comparison of Z-distributions obtained at $E_{lab}$ = 158 MeV and 248 MeV is given in Fig. 22. Note how the centroid of the Z-distribution shifts toward lower values as the excitation energy increases. The statistical model reproduces the experimental yields for residues of boron and heavier. It is not possible to unfold the spectra of lithium and beryllium ions because the direct

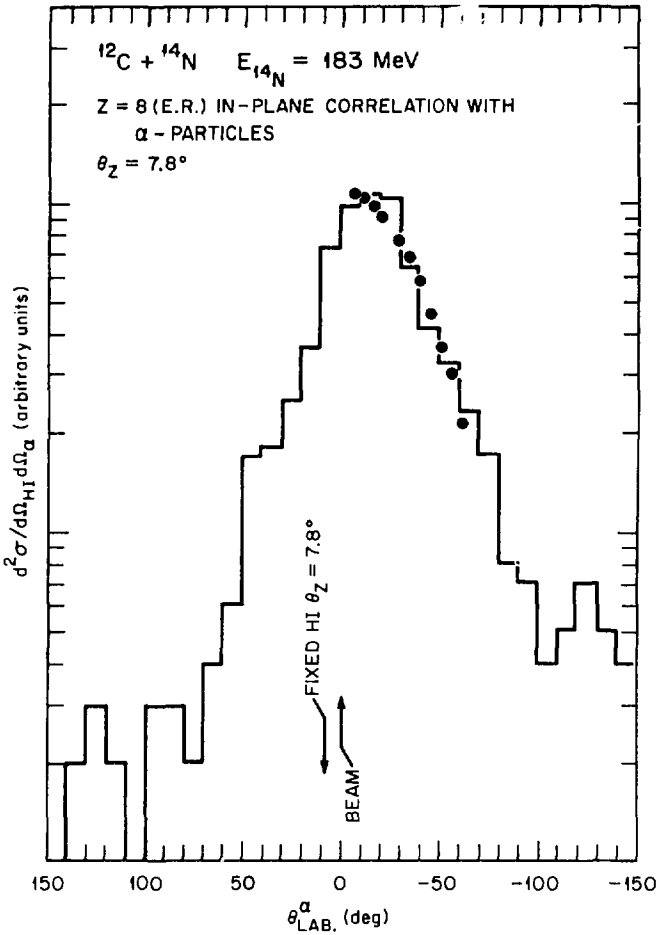


Fig. 20. The angular correlation of α-particles in coincidence with evaporation residues having Z = 8. The Monte Carlo calculation (histogram) is normalized to the data.

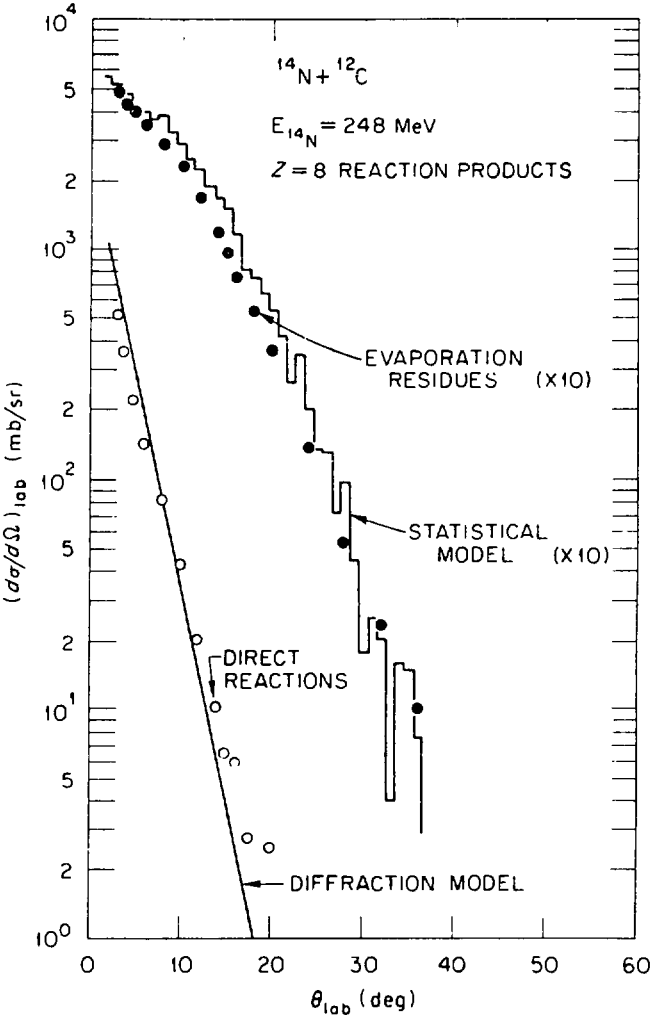


Fig. 21. The angular distribution of residues and of direct reaction products.

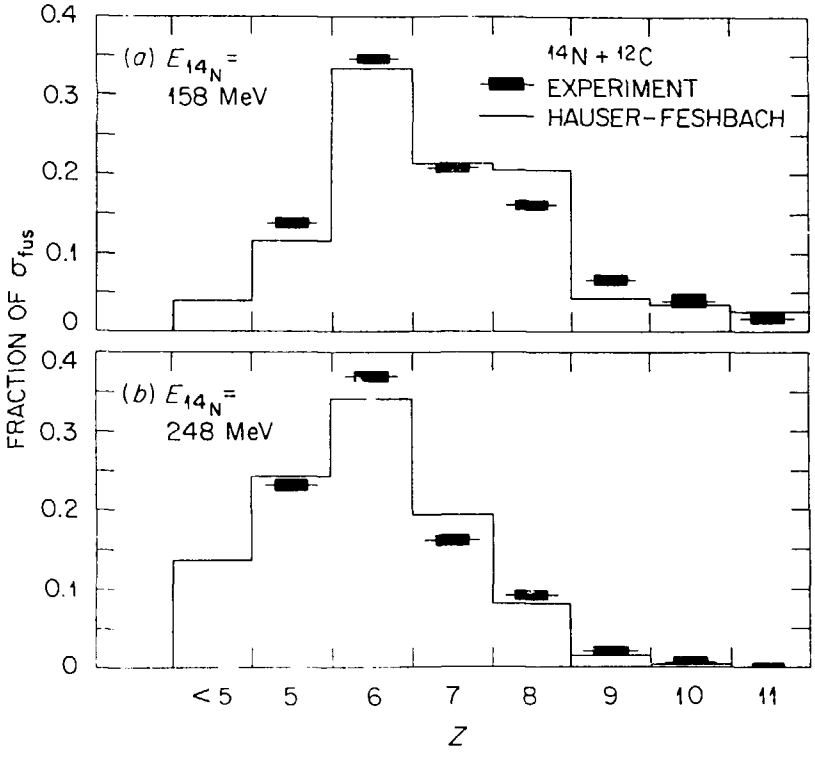


Fig. 22. The elemental distribution of residues obtained at two different bombarding energies.

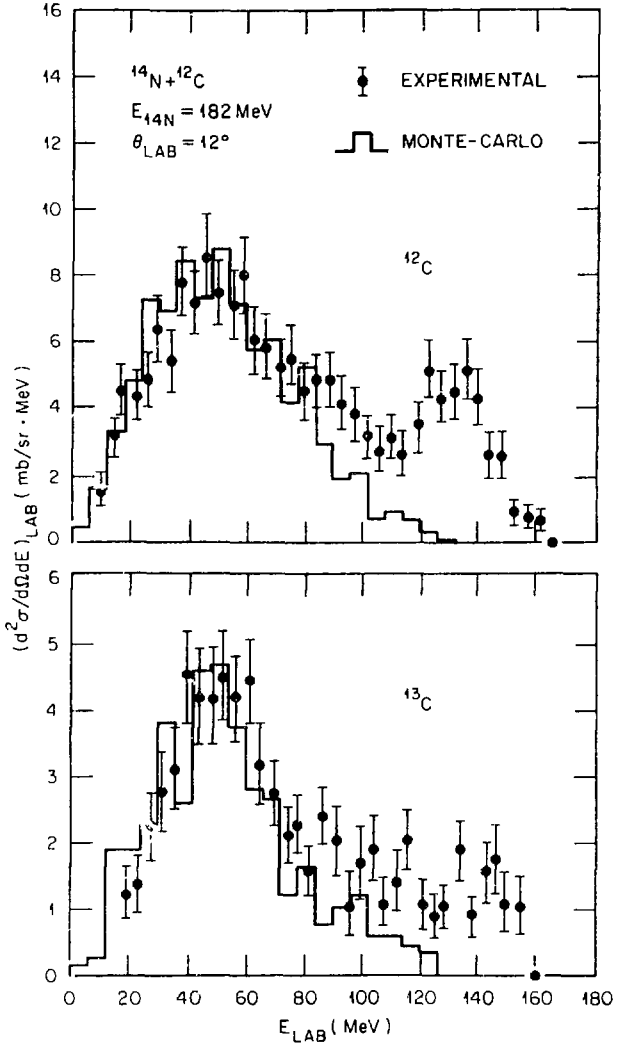


Fig. 23. The energy distributions of $^{12}C$ and $^{13}C$ obtained in a measurement of ΔE, E and time of flight. Note how the Monte Carlo reproduces the respective shapes of the evaporation residue portion of the yield.

reaction products and residues are not clearly separated in two peaks The statistical model is thus used to predict the small percentage of residues with $Z < 5$.

Additional information may be obtained by measuring the mass as well as the charge of a residue. Since the evaporation chains leading to different isotopes are different, differences in the shape of the energy spectra for the various isotopes are expected. Figure 23 shows the variation in shape for $^{12}C$ and $^{13}C$ residues. The slightly narrower distribution for $^{13}C$ is reproduced by the calculation. Angle integrated distributions are shown in Fig. 24. Only for the relative amounts of $^{11}B$ and $^{12}C$ is there a significant discrepancy in the angle-integrated yeilds. The predicted amounts of $^{11}B$ and $^{12}C$ depend critically upon the treatment of proton emission just above the threshold. Since the predicted yield of $^{12}C$ is too high by the same amount the $^{11}B$ yield is too low, we expect that this does not represent a serious discrepancy with the evaporation code and could be removed by a reasonable adjustment of the parameters affecting the proton decay of $^{12}C$.

It is possible to test the assumption of equilibrium without resort to a statistical model calculation by involving the independence hypothesis. Except for conserved quantum numbers such energy, angular momentum and possibly isospin, the decay of the compound nucleus should be independent of its formation. A comparison of the Z-distribution from the decay of $^{26}Al$ formed via $^{12}C + ^{14}N$ and $^{10}B + ^{16}O$ (Ref. 50) at two different energies is shown in Fig. 25. Note in each case that the excitation energies and angular momentum distributions (characterized by a maximum angular momentum $J_c$) are the same. The similarity of the Z-distributions is remarkable.

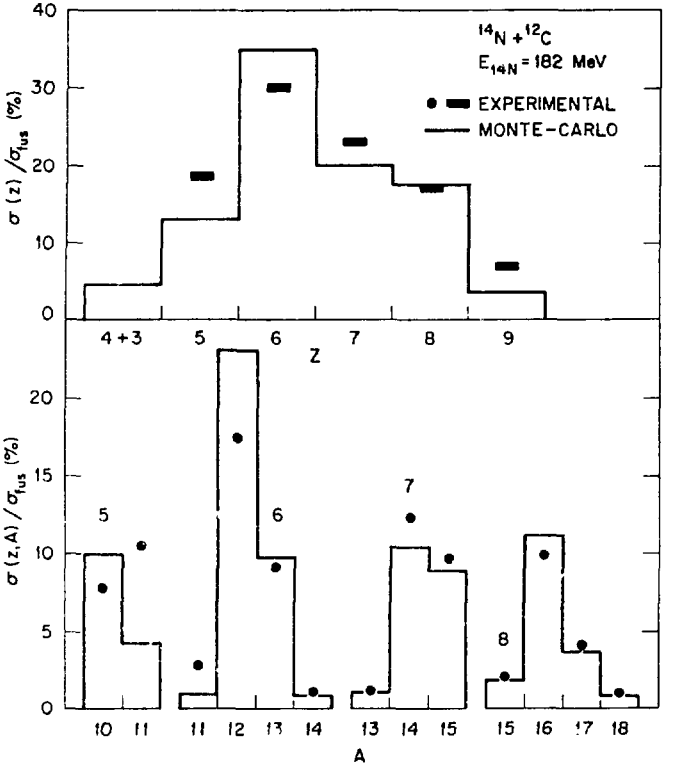


Fig. 24. Distributions of evaporation residues by element and isotope.

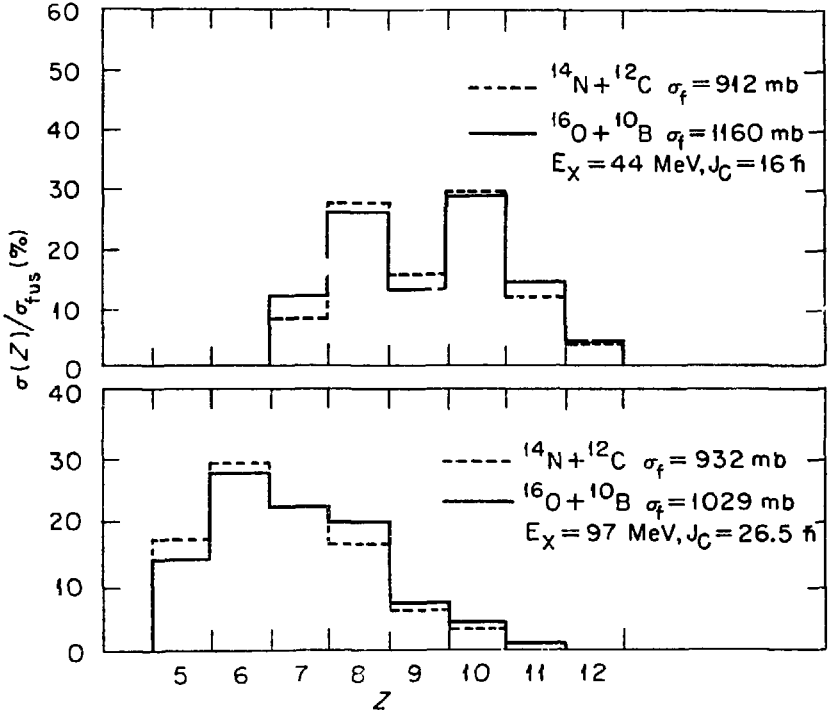


Fig. 25. Z-distributions of residues from two different reactions leading to the same compound nucleus. The respective bombarding energies have been chosen to yield compound nuclei at the same excitation energy and with the same distribution of angular momenta.

The double-peaked shape of the energy spectra observed at forward angles ( Fig. 18) has naturally lead to the classification of the reaction products into two categories - evaporation residues and direct reaction products. The sum of these two cross sections should give the total reaction cross section, provided no products have been lost (e.g. through detection thresholds) and there has been no double-counting of fragments. The total reaction cross section can be obtained through an optical model analysis of the elastic scattering. An example of this is shown in Fig. 26. The optical model fit to the data is excellent and yields a total reaction cross section $\sigma_R$ = 1400 mb. The energy dependence of $\sigma_R$ may be determined by an analysis at several energies and by comparision with a series of extensive measurements made on a similar system, $^{12}C + {}^{12}C$.[55]

A comparison of $\sigma_R$ obtained by adding $\sigma_{fus}$ and $\sigma_{direct}$ with $\sigma_R$ (optical model) is made in Fig. 27. The system $^{10}B + {}^{16}O$ is included in this comparison. Note the good agreement and, in particular, the relatively smooth behaviour of $\sigma_R$ in the high energy region. This is important in that it shows that reaction products are not escaping detection.

The above discussion has had two objectives. First to provide familiarity with the experimental data and method of determining $\sigma_{fus}$. Second, *and perhaps most importantly*, to give confidence that fusion cross sections can be reliably measured at such high energies. This confidence is indeed prerequisite for a discussion of the physical significance of the energy dependence of $\sigma_{fus}$.

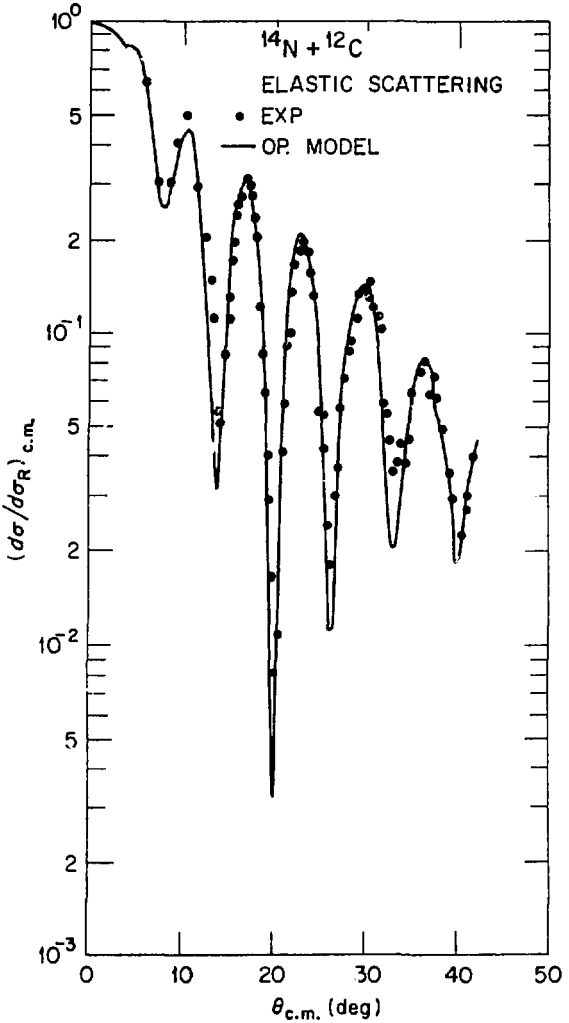


Fig. 26. The elastic scattering of $^{14}N$ by $^{12}C$ at an energy of 145 MeV lab. The optical model fit is used to obtain the total reaction cross section.

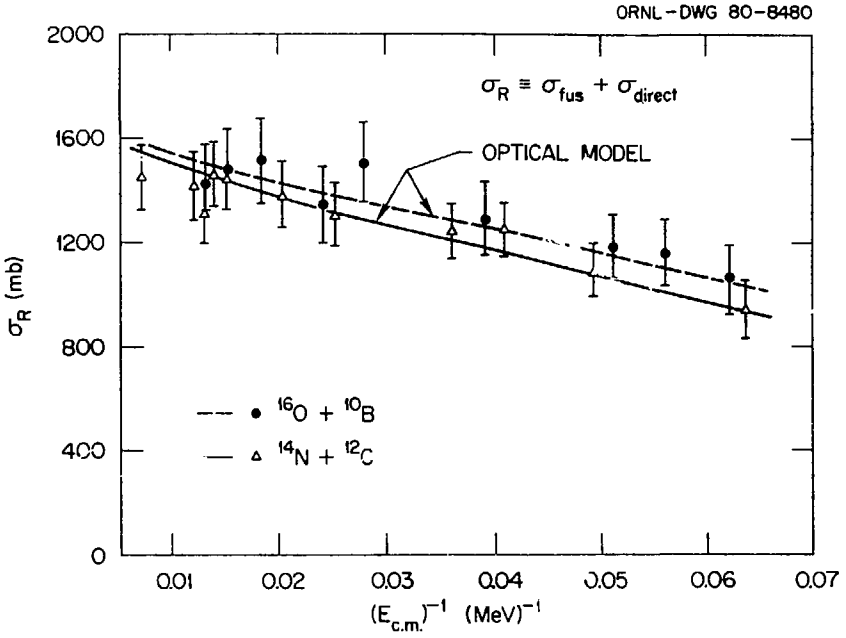


Fig. 27. The total reaction cross section for $^{10}B + ^{16}O$ and $^{12}C + ^{14}N$ obtained by adding the measured direct and compound components. The values obtained from optical model parameters based on fits to elastic scattering are shown.

## C. Experimental Results

Measurements of $\sigma_{fus}$ have been made for $^{12}C + ^{14}N$, $^{10}B + ^{16}O$ and, most recently, for $^{10}B + ^{14}N$ (Ref. 56). The results of these measurements are shown in Figs. 28-32. In cases where a critical angular momentum is shown, the value of J was determined with the sharp cutoff approximation (See Eq. 1)

$$(J + 1)^2 = \sigma_{fus}/\pi\lambda^2$$

and the excitation energy by

$$E_x = E_{c.m.} + Q$$

where Q represents the (positive) difference in binding energies between the entrance channel and the ground state of the compound nucleus.

Results for $^{12}C + ^{14}N$ reported by Conjeaud et.al.[46] and Kovar et.al.[34] are in good agreement with the present results in the lower energy region where a comparision is possible. A Saclay-Grenoble collaboration[57] has extended the Saclay measurements to higher energies and has obtained results in excellent agreement at $E_{^{14}N} \approx 100$ MeV.

A similar comparison with results from other laboratories is not possible in the case of $^{10}B + ^{16}O$. These results were obtained using the same methods and techniques as in the case of $^{12}C + ^{14}N$, however. At one particular bombarding energy, $E_{c.m.} = 41.2$ MeV, a $^{10}B$ beam and $^{16}O$ gas target were used. The kinematical properties of the evaporation residues in the lab system, as well as the method for determining the target thickness, are quite different. The consistency of this result with measurements at adjacent energies provides a valuable check.

The range of $^{14}N$ energy from 27-75 Mev has been covered by Parks et.al.[58] for the reaction $^{14}N + ^{10}B$ while the present work[56] ranges from 86 MeV to 180 MeV. The trends established by the data in these two regions appear consistent with one another. (See Figs. 31,32). Experimental data for the fusion of $^{12}C + ^{12}C$ (Refs. 34, 59) are also shown for comparison in Figs. 31 and 32.

## D. Discussion

Attempts to understand the behavior of fusion cross sections in light systems fall generally into two categories - those which emphasize either the properties of the projectile and target (the entrance channel) or those based on the properties of the compound nucleus. It should be clear that there is no physical reason why it must be an either/or situtation. The path from entrance channel to compound nucleus is continuous and the properties of the intermediate stages must also be important. (The two center shell model is a way of bridging the gap). Nevertheless the sharp separation of the two extremes has the great advantage of being convenient, not to mention possible, and it may provide essential clues.

The discussion of fusion reactions is often couched in terms of limitations on the fusion cross section or limitations on the critical angular momentum for fusion. Both the entrance channel and the compound nucleus place limits on fusion. At energies near the Coulomb barrier there are plenty of compound nuclear states available if they can be populated through the entrance channel. At very high energies the entrance channel may bring in an angular momentum larger than the compound nucleus can support, i.e.

*the compound nucleus does not exist and therefore is not formed.* At intermediate energies there must be a transition from one form of limit to the other. The questions are (i) which mechanism imposes the lower or more restrictive limit and (ii) what is the element of nuclear structure responsible for the limit.

### D. 1. Entrance Channel Models

The curved solid and dashed lines in Fig. 28 are fits to the data using Glas and Mosel's parametrisation. The parameters are ($^{12}C + {}^{14}N$, $^{10}B + {}^{16}O$) $r_B = (1.5, 1.5)$; $V(R_B) = (6.7, 6.7)$; $r_{cr} = (1.11, 1.35)$ $V(R_{cr}) = (-1.9, 2.5)$, $\hbar\omega = (2,2)$. Note the large difference in the reduced parameters describing the location of, and potential at, the inner critical radius. These parameter differences reflect the large differences for these two systems already apparent in Fig. 28 to the naked eye. Clearly, *the large variation in the cross sections are not explained by an* $A^{1/3}$ variation in nuclear radii.

Birkelund et. al.[12] have studied the systematics of fusion cross sections in the context of an entrance channel model. They solve the classical equations of motion for a real proximity potential and a proximity one-body frictional force. Without an ad hoc adjustment of parameters, they obtain reasonably good agreement for $^{12}C + {}^{14}N$. The prediction for $^{10}B + {}^{16}O$ is very similar to that for $^{12}C + {}^{14}N$ and therefore does not reproduce the data. This is not surprising since the global approach of their analysis excludes the variation of parameters to fit each case.

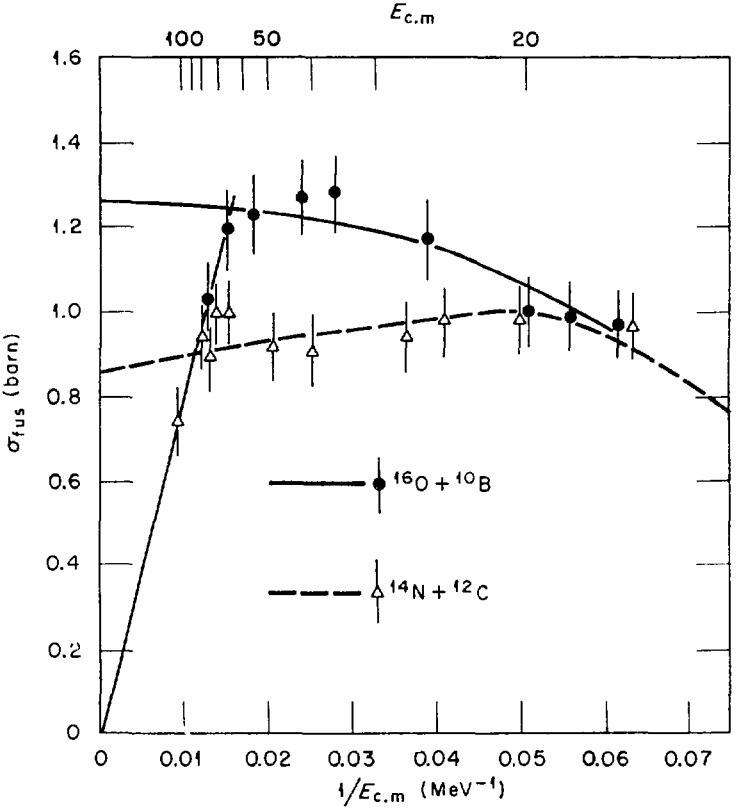


Fig. 28. Fusion cross sections plotted against $(E_{c.m.})^{-1}$ for $^{10}B + ^{16}O$ and $^{12}C + ^{14}N$. The solid and dashed curves are fits to the data using the parametrization of Glas and Mosel. The straight line passing through the origin gives the expected trend of $\sigma_{fus}$ for a constant maximum angular momentum of 27$\hbar$.

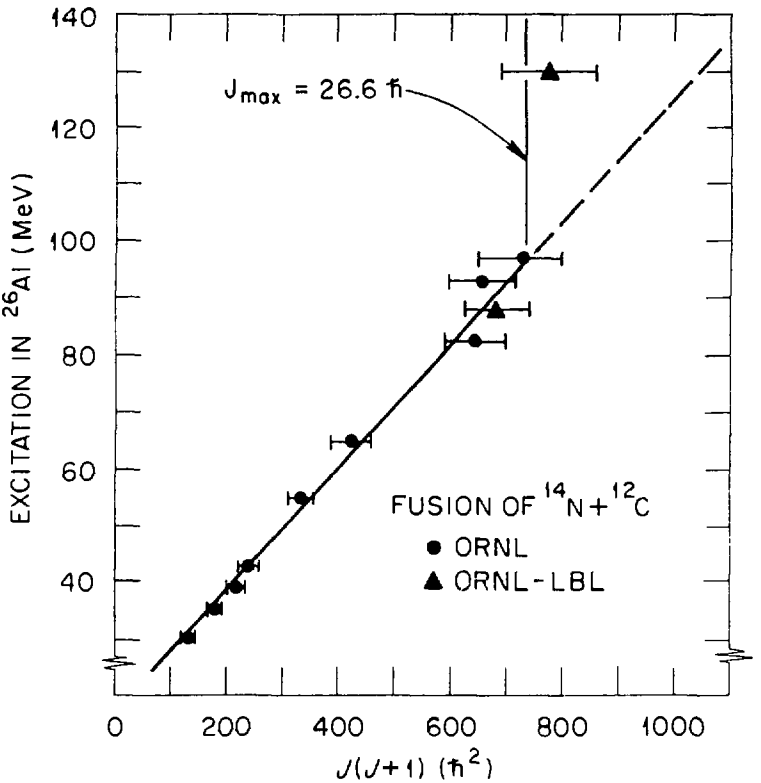


Fig. 29. Angular momenta obtained from $\sigma_{fus}$ for $^{12}C + ^{14}N$ by using the sharp cutoff approximation, as a function of excitation energy in the compound nucleus. The predicted location of the liquid drop limit is indicated.

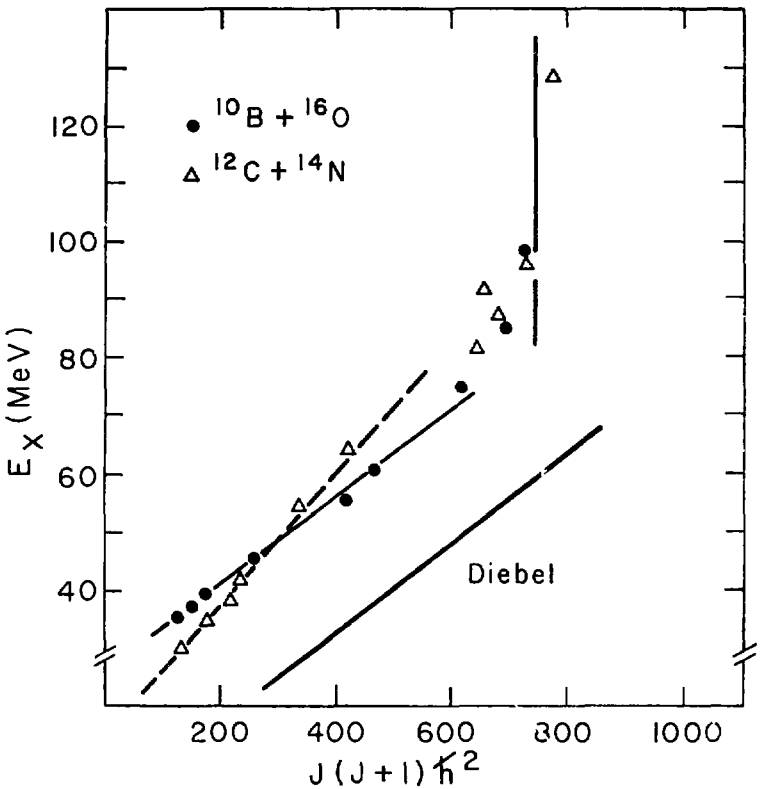


Fig. 30. Same as Fig. 29 but comparing $^{10}B + ^{16}O$ and $^{12}C + ^{14}N$. Note the different slopes of the loci for $J^2 \lesssim (25)^2\hbar^2$.

Nuclear radii do not vary exactly as $A^{1/3}$, however, and the effects on this on the fusion cross section can be estimated. Folding model calculations,[1] which incorporate mean-square radii determined by electron scattering, indicate that $^{12}C + ^{14}N$ and $^{10}B + ^{16}O$ have the same mass overlap at radii of 1.11 and 1.15 times $(A_1^{1/3}+A_2^{1/3})$, respectively. Incorporating this in the Glas and Mosel formulation produces a maximum predicted difference in the cross section of 7%. While ir the right direction, this accounts for about only one-fifth of the observed difference.[50]

Vandenbosch[60] has calculated fusion cross sections with a classical trajectory model incorporating the proximity potential and one-body friction (similar to Birkelund et. al.[12]) but has used radii and diffusness parameters taken from electron scattering results. These calculations predict differences between $^{10}B + ^{16}O$ and $^{12}C + ^{14}N$ which are from one-third to one-half of the observed differences. However, the overall energy dependence is not well reproduced.

From the above we may conclude (for $^{12}C + ^{14}N$ and $^{10}B + ^{16}O$) that either the entrance channel is not the most important limiting factor for fusion in the region of $E_{c.m.}$ 20-70 MeV, or, if the entrance channel is the important factor, then individual nucleons may be playing a critical role in a way not described by macroscopic calculations.

The experimental data compared for $^{12}C + ^{12}C$ [4,59] and $^{10}B + ^{11}N$ [56,58] in Fig. 31 appear to behave qualitively differently than the $^{10}B + ^{16}O$ and $^{12}C + ^{14}N$ systems in Fig. 28. In this case (Fig. 31), the cross sections for the two systems are comparable at the same center of mass energies. One must realize that there are some discrepancies in the data (e.g. for $^{12}C + ^{12}C$ at $E_{c.m.} \approx (0.045)^{-1}$ MeV) and that four different groups at as many different laboratories have contributed results. Furthermore, the methods employed in unfolding the data to determine $\sigma_{fus}$ are not identical. With this important caveat, however the combined results presently available suggest that difference in $\sigma_{fus}$ at the same

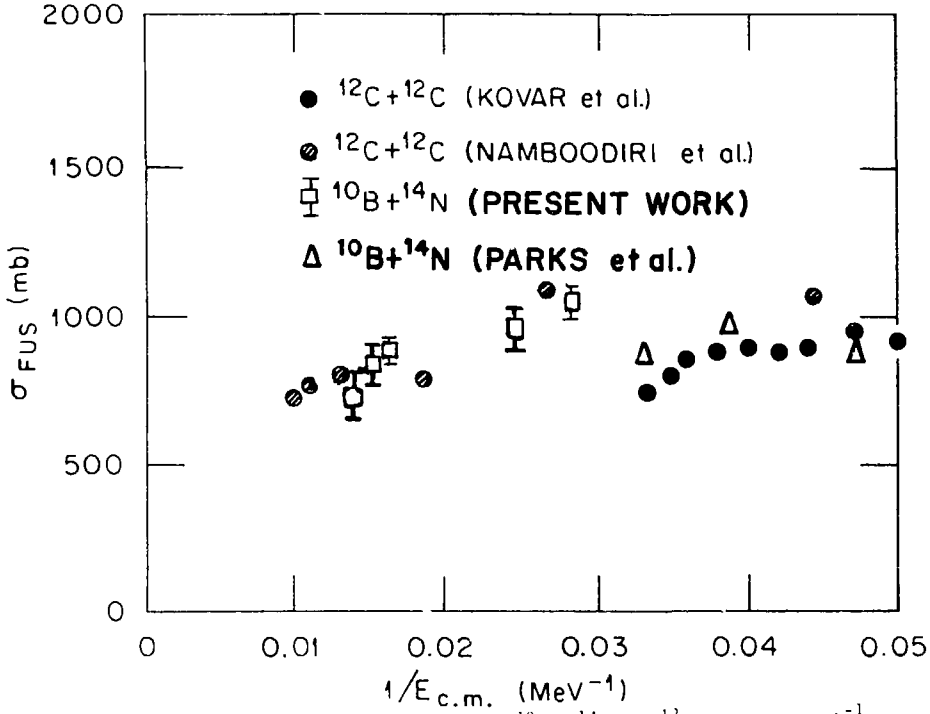


Fig. 51. Fusion cross sections for $^{10}B + ^{14}N$ and $^{12}C$ versus $(E_{c.m.})^{-1}$.

$E_{c.m.}$ for these two systems, both leading to $^{24}Mg$, are small, in spite of the markedly different structures of $^{10}B$, $^{12}C$, and $^{14}N$. Entrance channel models would be able to explain this particular behavior (Fig. 31) without recourse to nuclear structure effects.

D. 2. Compound Nucleus Models

Just as the entrance channel is characterized by the bombarding energy $E_{c.m.}$ and $\sigma_{fus}$, the compound nucleus is described by its excitation energy $E_x$ and its maximum angular momentum J. Figures 30 and 32 show $E_x$ vs J(J+1) for the compound nuclei $^{26}Al$ and $^{24}Mg$, respectively. If, for example, the compound nucleus were the limiting factor on $\sigma_{fus}$ at all energies (and for all entrance channels), then all the data points in Figs 30 and 32 should determine a single locus. This is clearly not the case. At low excitation energies we expect differences because the Coulomb barrier (or outer interaction barrier) is the important factor. At high energies, the liquid drop limit should set in[44,48], and this is apparent in Figs. 29 and 30 but not in Fig. 32. I will come back to this "ultimate" limiting angular momentum later, and want to discuss now the intermediate energy region.

It is clear that the limiting angular momenta for $^{12}C + ^{14}N$ and $^{10}B + ^{16}O$, and also for $^{10}B + ^{14}N$ and $^{12}C + ^{12}C$ each determine separate loci. In Fig. 30 the loci cross: in Fig. 32 they seem parallel. Thus, strictly speaking, the compound nucleus cannot be the limiting factor for <u>both</u> $^{12}C + ^{14}N$ and $^{10}B + ^{16}O$. A similar statement holds for $^{10}B + ^{14}N$ and $^{12}C + ^{12}C$. The compound nucleus <u>could</u> be the limiting factor when $^{12}C + ^{12}C$ is the entrance channel, but not for $^{10}B + ^{14}N$.

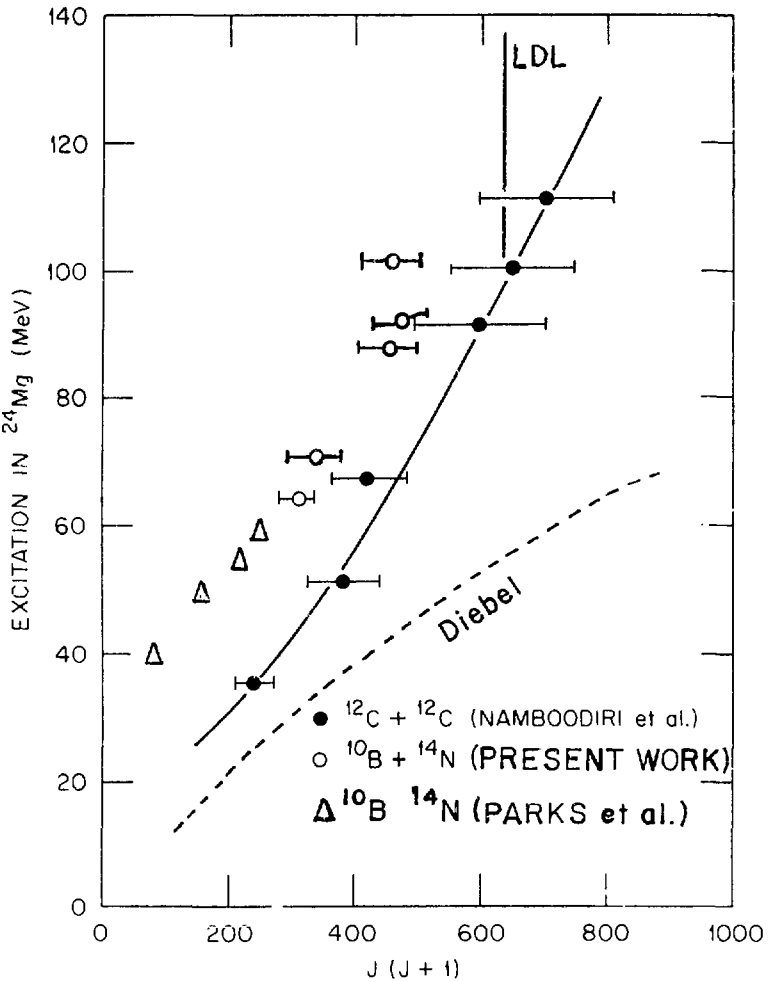


Fig. 32. A comparision of angular momentum versus excitation energy for $^{10}B + ^{14}N$ and $^{12}C + ^{12}C$.

It is true that the differences between $^{10}B + ^{16}O$ and $^{12}C + ^{14}N$ shown in Fig. 28 appear smaller when the data are plotted as $E_x$ vs. $J(J+1)$. A contributing factor to this is the $\sim 4$ MeV difference in Q values for the two reactions.† The Saclay group[61] has examined a number of different reactions leading to the same compound nucleus and finds, in general, that the differences in Q-value are in the direction such that an $E_x$ vs. $J^2$ plot produces loci closer to each other than in the case when the data are plotted as $\sigma_{fus}$ vs. $E_{c.m.}$ This trend has been noted in another form, viz., the variation of $\sigma_{fus}^{max}$ from system to system, by Lee et.al.[62]

While it is generally useful to search for quantities which correlate the trends of many results, at least two serious problems confront this approach. The first is the crossing (for different slopes) of the loci shown in Fig. 30, for no Q-value shift can eliminate that and, second,the shifted loci shown in Fig. 32 for $^{10}B + ^{14}N$, and $^{12}C + ^{12}C$. Here, the effect of the Q-value difference is to move apart the loci which are similar in the $\sigma_{fus}$ vs $E_{c.m.}$ plot.

If it were possible to know independently the location of the Yrast line, then it would be obvious whether the entrance channel or the compound nucleus is the limiting factor. To obtain guidance from theory is a step in this direction. Glas and Mosel[63] have used the Strutinsky method for rotating nuclei to calculate Yrast lines in the mass region from A = 24-60. Their results for A = 26 and A = 24 are indicated in Figs. 30 and 32. It is thus clear that fusion reactions do not populate (and therefore are not limited by) the Yrast line of a rapidly rotating, highly deformed, but otherwise "cold" nucleus. The nuclear system produced in a high energy

†A mathematical (as opposed to a physical) factor making the differences shown in Fig. 30 appear smaller is the square-root dependence of J on $\sigma_{fus}$.

collision will have some thermal excitation and therefore be removed from the cold Yrast line. It appears reasonable that the structure of the cold Yrast line is carried over to an effective Yrast line relevant for fusion. This approach has been followed by Lee et. al.[62] who assume that the effective Yrast line lies parallel to the cold Yrast line. A fit to a number of data suggests that the shift is $\sim$ 10 MeV if the cold Yrast line is calculated with a right body moment of inertia having a radius parameter $r_o$ = 1.2 fm. However, there are significant deviations between experiment and this parametrisation, and the measured slopes of $\sigma_{fus}$ are not always reproduced.

Another method of defining an effective Yrast line has been proposed by Vandenbosch.[64] The argument is made that fusion will occur when the compound nucleus is far enough above the Yrast line such that the average width of levels $\Gamma$ divided by the average spacing is the order of unity. The value of $\Gamma$ is obtained from the empirical correlation of experimental values given by Shapira et. al.[65] and the spacing of levels from the compilation of Gilbert and Cameron.[66] The location of the effective Yrast line determined this way and the fusion cross sections determined by it are shown in Fig. 33 a,b. (There is an uncertainty in the location of this line connected with the uncertainty in the density of levels). The comparision with experiment is favorable, particularly for the higher J values. At lower J-values, $J \lesssim 20$, the data lie further above the Yrast line. As noted by the authors,[64] this suggests that the properties of the entrance channel are the more stringent limiting factor for bombarding energies just above the break in $\sigma_{fus}(E)$. This interpretation may be contrasted with that of Lee et. al.[62] who would extend the validity of their statistical Yrast limitation down to energies at which $\sigma_{fus}^{max}$ is reached. The data for $^{10}B + {}^{14}N$ would be in strong disagreement with such a prediction.

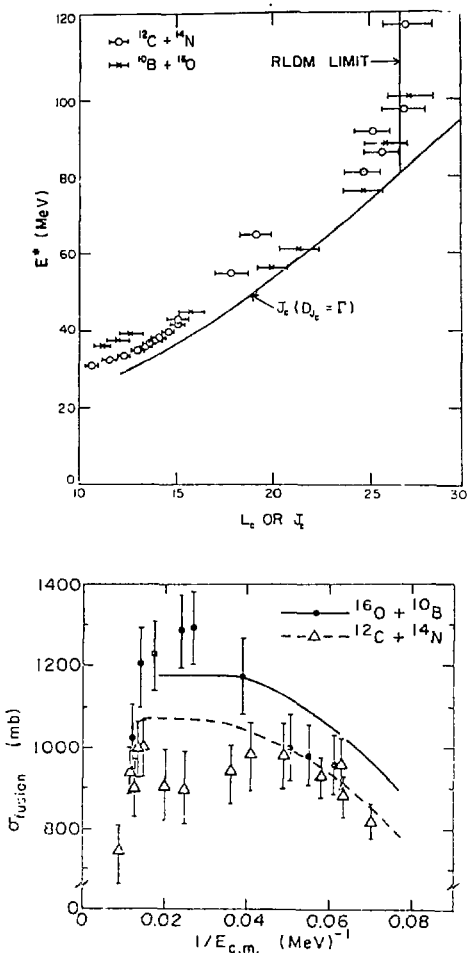


Fig. 33. a) The location of an effective Yrast line defined by $\Gamma/D = 1$ and b) the fusion cross sections predicted by such an angular-momentum limitation. From Vandenbosch and Lazzarini.[64]

D. 3. Synthesis

The question "limitations to fusion -- entrance channel or compound nucleus?" thus may have no simple answer in the intermediate energy region. The variety of experimental data available, particularly for systems leading to the same compound system, has increased rapidly in the last five years. With this have come significant improvements in our understanding of and appreciation for the complexity of the situation. Given the data shown in Fig. 32, it is apparent that $^{10}B + ^{14}N$ cannot be limited by the Yrast line of the compound nucleus. On the other hand, the general success with which trends in maximum fusion cross sections and variations in energy dependence correlate with the Q-value for compound nucleus formation suggests that an effective Yrast line may be an important factor in entrance channels having tightly bound nuclei.

The above discussion has focussed on fusion and has neglected the process which competes with it for the flux making up the total reaction cross section. This process is the direct or peripheral reaction. The elements of nuclear structure (presense of collective levels, etc.) and reaction mechanism governing the strength of the direct reaction channels are of equal importance in understanding fusion cross sections. Efforts to approach the question of fusion from this point of view are promising.[15,67,68]

It seems likely that a future understanding of the fusion cross sections for light systems will have to encompass both the entrance channel (including competition with the direct reactions) and the properties of the compound and pre-compound states.

To conclude this section I would like to come back to the matter of the rotating liquid drop limit - the colloquial name for the maximum angular momentum a nucleus can have without fissioning. This is in a real sense a fundamental quantity. The data for $^{12}C + ^{14}N$ and $^{10}B + ^{16}O$ exhibit such a maximum angular momentum.[†] The value[48] of this angular momentum (see Fig. 29) is consistent with that of the rotating liquid drop model.[44] It is interesting to consider the predicted shape of the $^{26}Al$ nucleus at this limit. The dashed line in Fig. 34 shows the shape of the saddle point configuration and the solid line that of the ground state configuration At 26 ħ the shapes are nearly identical. (At 26.6 ħ they are identical). The configuration at the liquid drop limit is very similar to that of a carbon and nitrogen ion in close contact. Thus in this limit the concept of compound nucleus and entrance channel merge.

### D. 4. The Low-ℓ Window

An interesting feature in the mechanism for fusion has been predicted by time dependent Hartree-Fock calcualtions.[4] Above a certain energy threshold, ions colliding with a small impact parameter do not lead to fusion. Instead, the ions (or fragments with nearly the same mass) reemerge with a reduced relative kinetic energy. The maintainance of coherence of the nuclear wave functions, which allows the system to come apart, is a consequence of the mean field approximation and the absence in the cacleulation

[†] The data for $^{12}C + ^{12}C$ and $^{10}B + ^{14}N$ do not indicate a common liquid drop limit. It is important to extend measurements for both systems to higher energies and to perform similar measurements and analyses on each system.

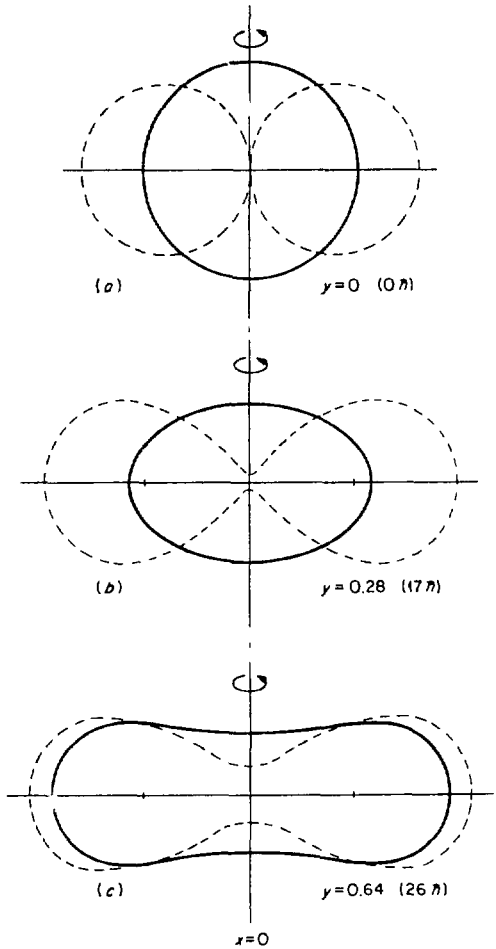


Fig. 34. The shapes of a nucleus with A ∿ 26 as predicted by the rotating liquid drop model.[44]

of two-body nucleon-nucleon collisions. At larger impact parameters, initial relative kinetic energy can be converted into rotational energy and fusion is possible. At still larger impact parameters, centrifugal forces prevent fusion. Thus a window in $\ell$ space arises, having a low $\ell$-cut off and high $\ell$ cutoff.

The Z and A distribution of the evaporation residues is sensitive to the distribution of angular momenta in the compound nucleus. High angular momenta favor $\alpha$-emission and consequently lighter residues. Low-$\ell$ values preferentially populate the heavier residues through nucleon emission. This fact has been exploited by a number of workers to search for the presense of a low-$\ell$ window. To date all searches have yielded negative results. Some of the systems which have been studied are $^{16}O + ^{16}O$ (Refs. 69-71) and $^{27}Al + ^{28}Si$ (Ref. 72). The analysis of evaporation residues from $^{10}B + ^{16}O$ and $^{12}C + ^{14}N$ described in section B extends over a wide range of bombarding energies above and below the predicted threshold for the low-$\ell$ cutoff. The analysis was done with a triangular $(2\ell+1)$ distribution extending from $\ell_c = 0$ to $\ell_{max}$ and it reproduced the data quite well.[47-50] An analysis of these data in terms of $\ell_c > 0$ (similar to that of Refs. 69, 72) is in progress.[73]

Coincidence measurements designed to detect the low energy fragments from a non-fusing central collision may prove to be more sensitive to the presense of a low-$\ell$ window. Several experiments and analyses are in progress at the moment on $^{16}O + ^{16}O$ (Refs. 74-75) and on $^{12}C + ^{14}N$ (76).

## V. The Effect of Nuclear Deformation

### A. Motivation

The static or equilibrium shapes possessed by nuclei as well as the collective motions they undergo are major subjects in the study of nuclear structure. A variety of experimental techniques using different nuclear probes has resulted in a detailed knowledge of the quadrupole and hexadecapole moments and quadrupole vibrational strengths of nuclei throughout the periodic table. The isotopes of Sm provide a particularly interesting opportunity for the study of nuclear structure and how this structure is reflected in various reaction mechanisms. Figure 35 shows the energies of the first $2^+$ states and the quadrupole transition strengths connecting these states to the ground state. The Sm isotopes thus undergo a transition from spherical (vibrational) to deformed (rotational) behavior. The effect of nuclear deformation on heavy-ion fusion can thus be studied by measuring an excitation function for $\sigma_{fus}$ for the same projectile and the different isotopes. This has been done for $^{16}O$ (Ref. 77,78) at the Weizmann Institute and for $^{40}Ar$ projectiles[79] at GSI. The results exhibit the effect of nuclear deformation on fusion, but a quantitative analysis shows the current theoretical methods for describing the reaction mechanism are not entirely adequate, and, furthermore, suggests that other degrees of freedom (e.g. neck formation) are important.

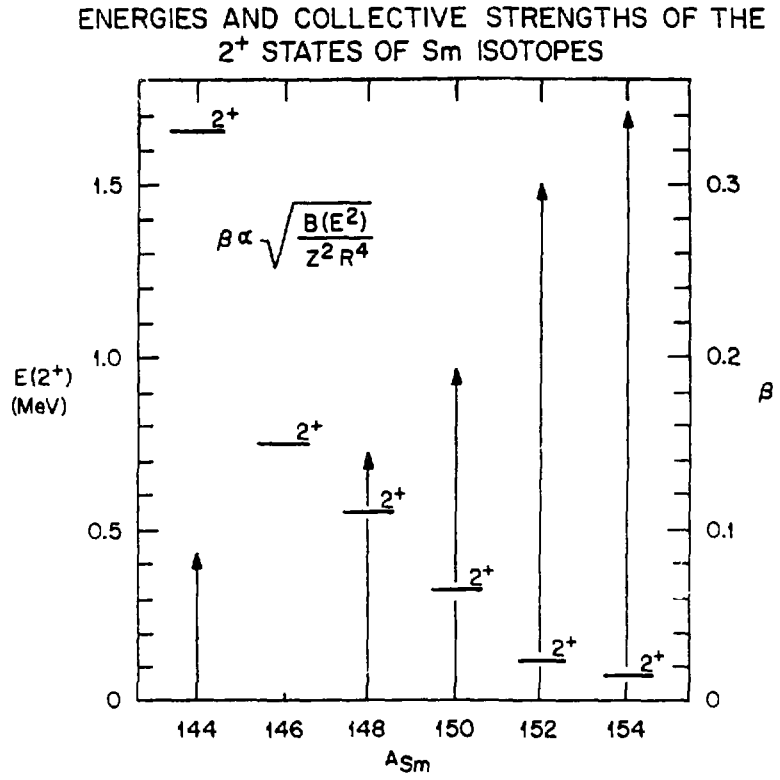


Fig. 35. The energies of the first excited states of the even-even Sm nuclei and the parameter $\beta$ describing the quadrupole collectivity.

## B. Experimental Method

Since cross sections at energies well below the barrier are very small, the experimental method must be capable of detecting with good precision small quantities of evaporation residues. Since an in-beam measurement would be complicated by γ-rays from Coulomb excitation and from contaminants it was decided to make an off-line observation of the x-rays from the radioactive evaporation residues trapped in the catcher foil. A schematic of the experimental apparatus is shown in Fig. 36. The surface barrier detectors monitored the beam during the irradiation so that an absolute normalization could be obtained without having to make an independent measurement of the target thickness. The catcher foils located downstream from the target were made of carbon for $^{16}O$ bombardment of Al in the case of $^{40}Ar$. The thicknesses were chosen just adequate to stop all the desired residues. In this way radioactive products from reactions with light contaminants in the target, and with the atoms of the catcher foil itself, were not retained. This produced a low background, as shown in Figure 37. This particular spectrum was obtained in 10 minutes of counting after a one-hour long bombardment. The cross section for fusion of $^{16}O + ^{150}Sm$ at 60 MeV (lab) is about 500 microbarns. The smallest cross section measured was ≈ 100 microbarns.

In order to obtain absolute cross sections, it is necessary to know the number of x-rays emitted per disintegration by each of the various isotopes contributing to the measured yield. Such values can be obtained if the decay scheme has been studied previously and an absolute normalization has been determined. Much work has been done on decay schemes for

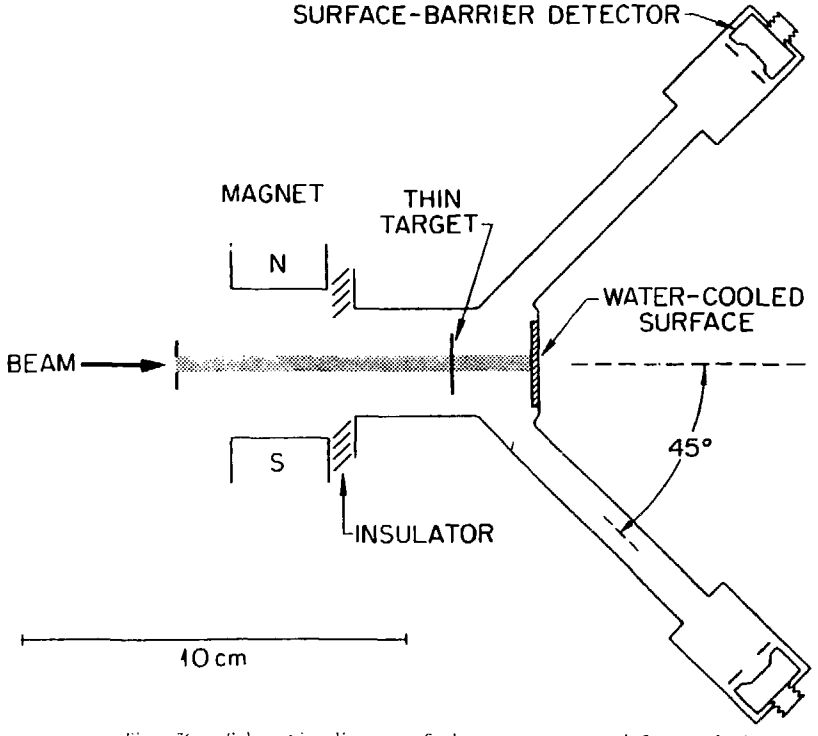


Fig. 30. Schematic diagram of the apparatus used for producing evaporation residues and trapping them in catcher foils. The latter are indicated by the diagonal lines shown next to the water-cooled surface.

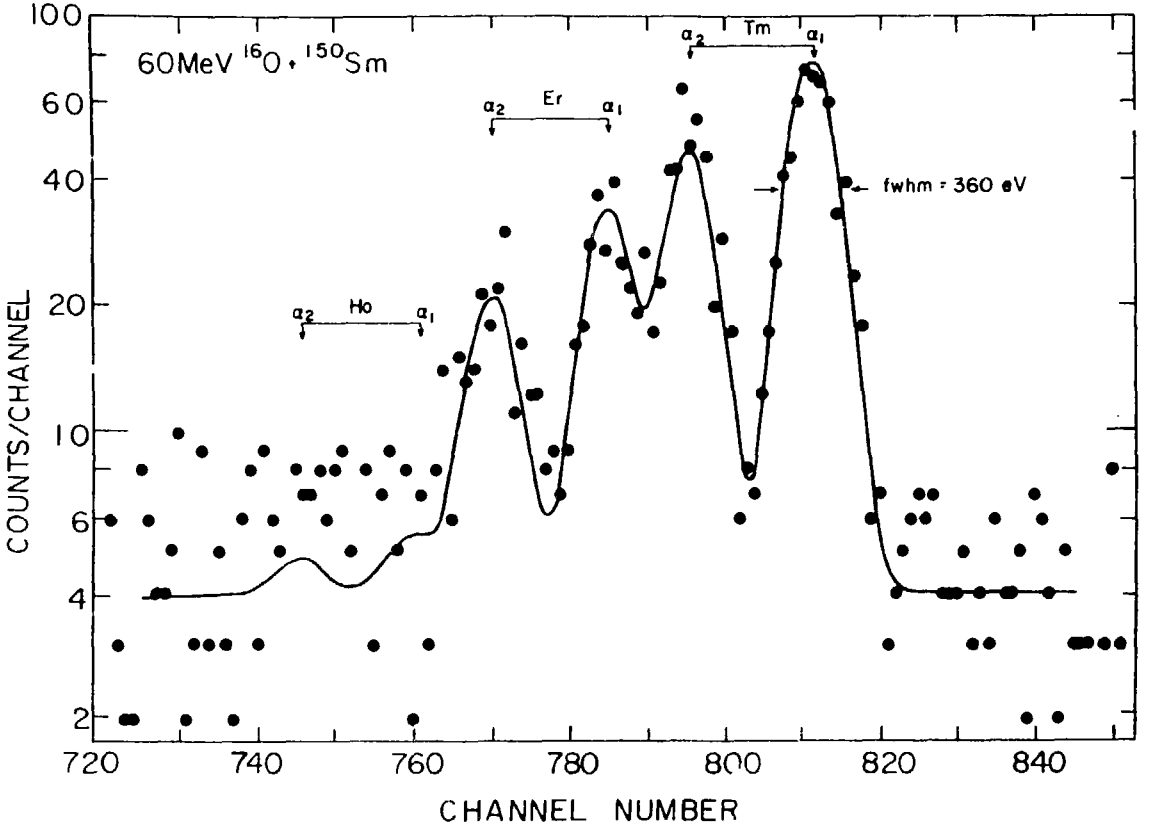


Fig. 37. Photon spectrum covering the range from 45-55 keV. The Tm $K_{\alpha 1}$ and $K_{\alpha 2}$ x-rays are produced by the electron capture decay of Yb and subsequent internal conversion in the Tm daughter. The full curve is a fit to the data in which each component is approximated by a Gaussian.

neutron deficient isotopes in the last decade and evaluated level schemes have been prepared by the Nuclear Data Project at Oak Ridge National Laboratory. From this information it is possible to calculate the number of x-rays originating from electron capture (the shaded areas in Fig. 38) and from the subsequent internal conversion of nuclear transitions (unshaded areas). The individual values shown in Fig. 38 for the decay of isotopes produced by the fusion of $^{16}O$ + Sm are estimated to have an accuracy of ±10%. Note that typically 80 $K_{\alpha}$ x-rays are obtained per 100 decays of an isotope. Similar information has been compiled for the decay of the Hg isotopes produced by Ar + Sm. Since this relatively high yield can be detected with 25-10% efficiency with a Ge spectrometer, the method is ideal for measuring small cross sections.

Information on the distribution of isotopes produced in the fusion reactions is contained in the time dependence of the delayed x-ray yield. Figures 39 and 40 show a typical case. Parent, daughter and granddaughter activities are observed. The full curves are fits to the data in which the know half-lives and absolute x-ray intensities of each isotope were incorporated. The contributions of the individual isotopes, produced by the evaporation of 2, 3, or 4 neutrons from the $^{166}Yb$ compound nucleus, are indicated in Fig. 40. From analyses such as this the isotopic distributions shown in Fig. 41 were obtained. They exhibit the behavior expected for evaporation of neutrons from an equilibrated compound nucleus (charged particle emission in these cases is fairly small). Some comparisons with statistical model calculations have been made and they show reasonably good agreement with experiment.

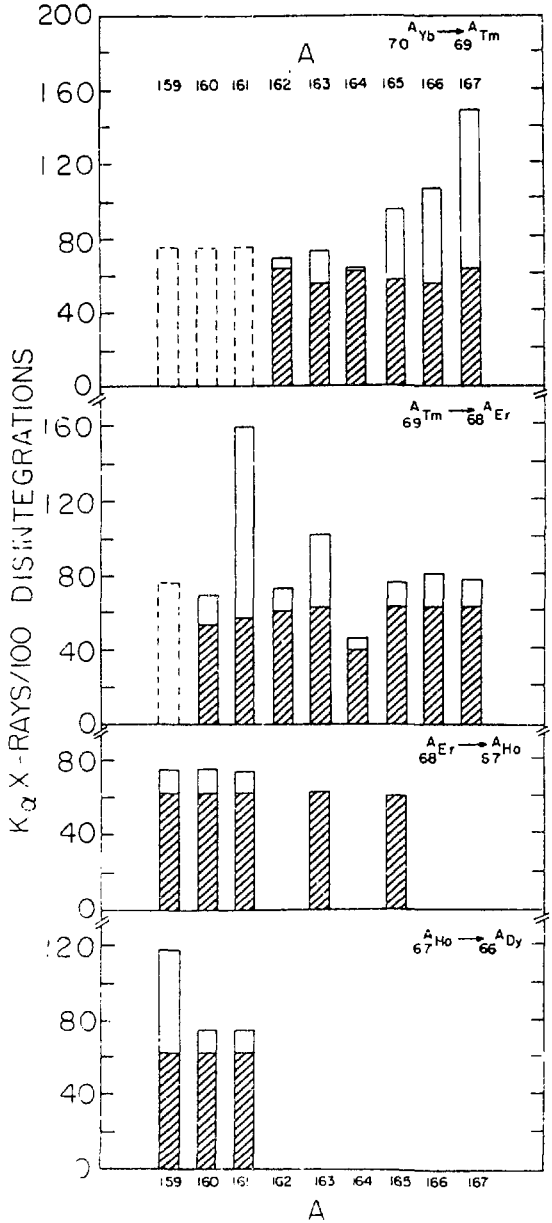


Fig. 38. Resolute γ ray intensities from the decay of various isotopes produced in the fusion of $^{16}O$ + Sm.

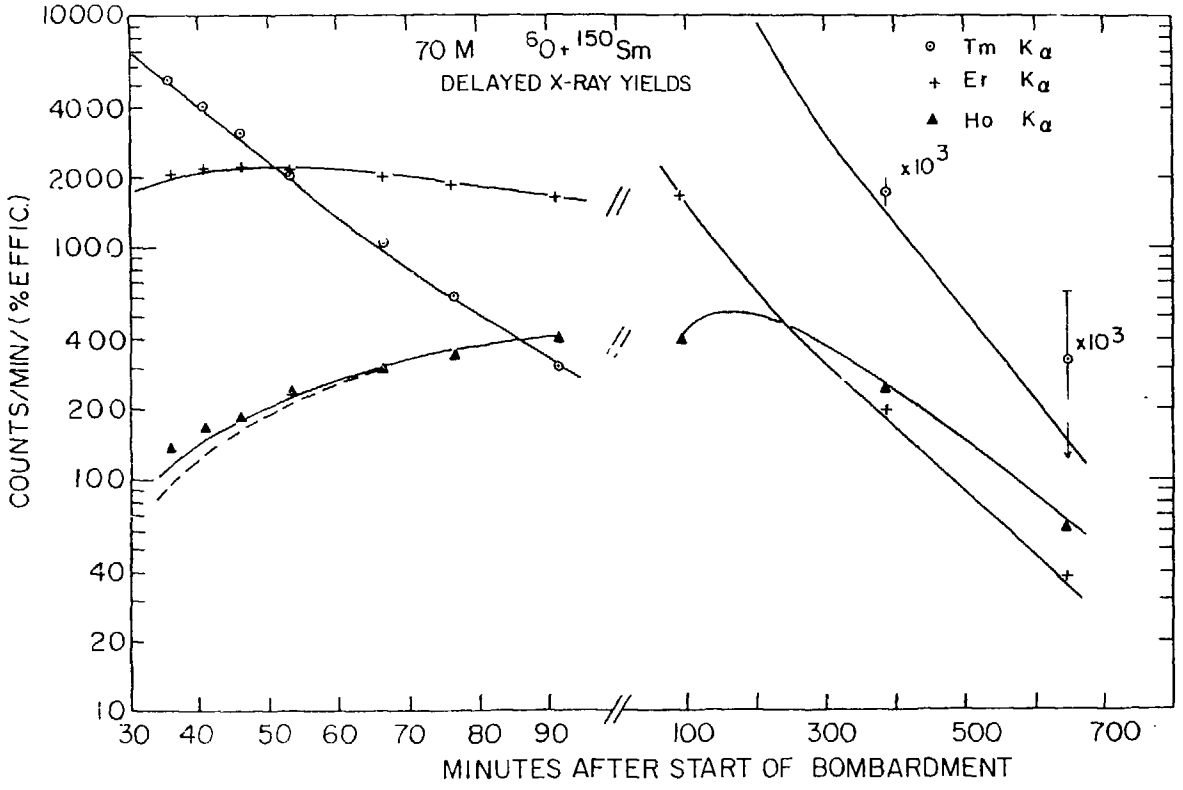


Fig. 59. The X-ray count rate as a function of time. The length of the bombardment was 28 minutes. The full curves are fits to the data incorporating known half-lives and absolute X-ray intensities.

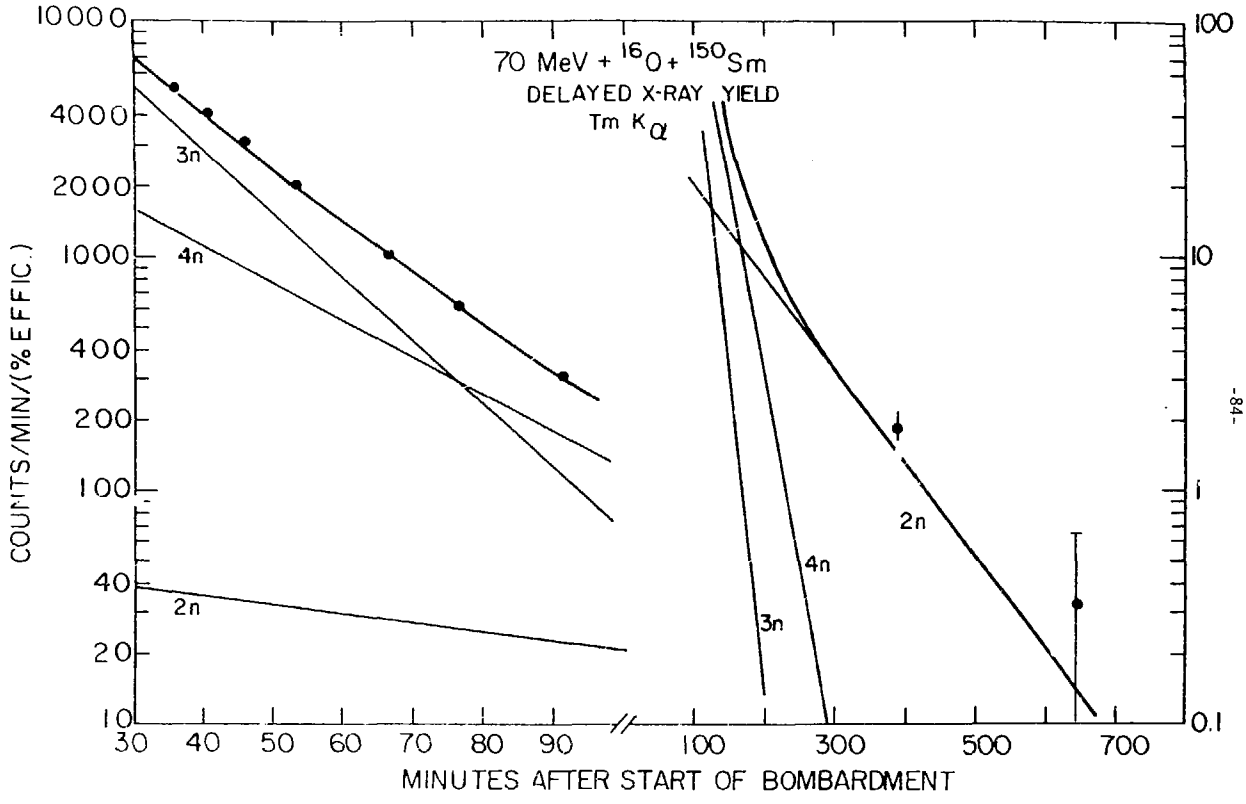


Fig. 40. The time dependence of the parent activity and the deduced contributions of the 2n, 3n and 4n activities. Note that measurements at later times effectively determine the 2n portion.

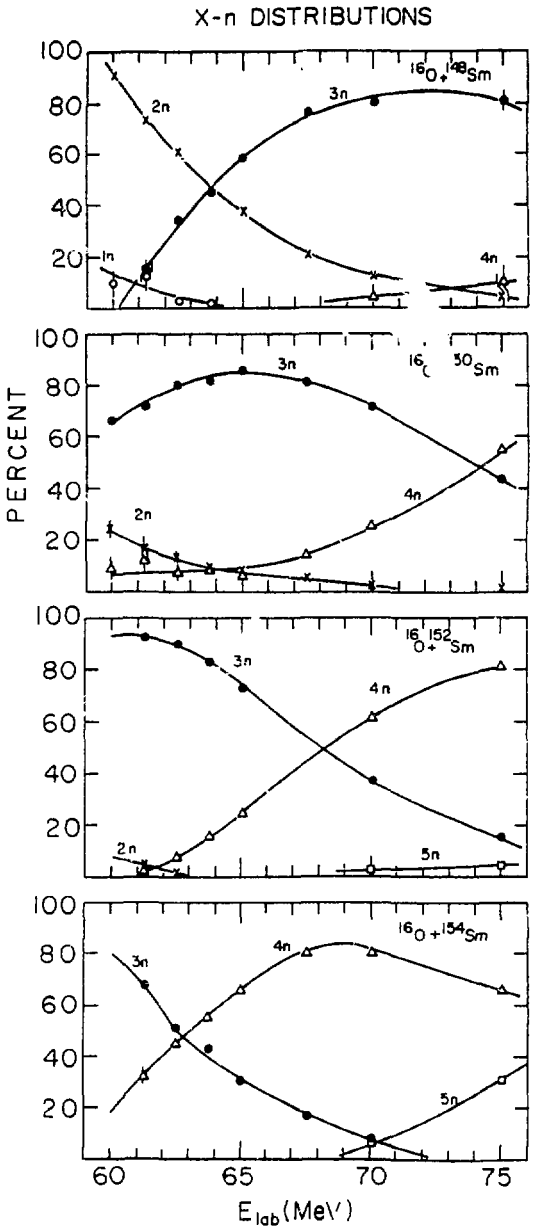


Fig. 41. The distribution of the evaporation residues as a function of bombarding energy for the four systems studied. The value of n denotes the number of mass units evaporated by the compound nucleus. The yields are expressed as a percentage of the total fusion cross section. The lines are only to guide the eye.

The cross sections for the production of evaporation residues are shown in Figs. 42, and 43. The error (random plus systematic) on a data point is typically ±10% in Fig. 42 and ±15% in Fig. 43. Since fission competition is negligible for the Yb residues produced at the relatively low bombarding energies here, the evaporation residue cross sections in Fig. 42 ($^{16}O$ + Sm) are equivalent to the fusion cross section. This is not the case for $^{40}Ar$ + Sm and it was necessary to measure the fusion-fission yield in a separate experiment using a ΔE-E counter telescope. When this contribution is added to the evaporation residue yield, the fusion cross sections shown in Fig. 44 are obtained.

## C. Results

The fusion cross sections shown in Figs. 42 and 44 exhibit variations which become relatively larger as the bombarding energy is lowered. These variations, we shall see, are far in excess of the changes expected for spherical, structureless nuclei whose radii increase simply as $A^{1/3}$.

## D. Discussion

Since the motivation of these experiments was to study the effect of nuclear structure on the fusion of heavy ions, let us consider in more detail the structural aspects of the even-even Sm isotopes shown in Fig. 35. The energy of the first $2^+$ state drops rapidly from its value of 1.65 MeV at the N = 82 closed neutron shell of $^{144}Sm$ to a minimum of 82 keV for $^{154}Sm$. Accompanying this rapid change is a strong increase in the quadrupole deformation parameter $\beta_2$ which has been evaluated from the electric quadrupole transition matrix element connecting the ground

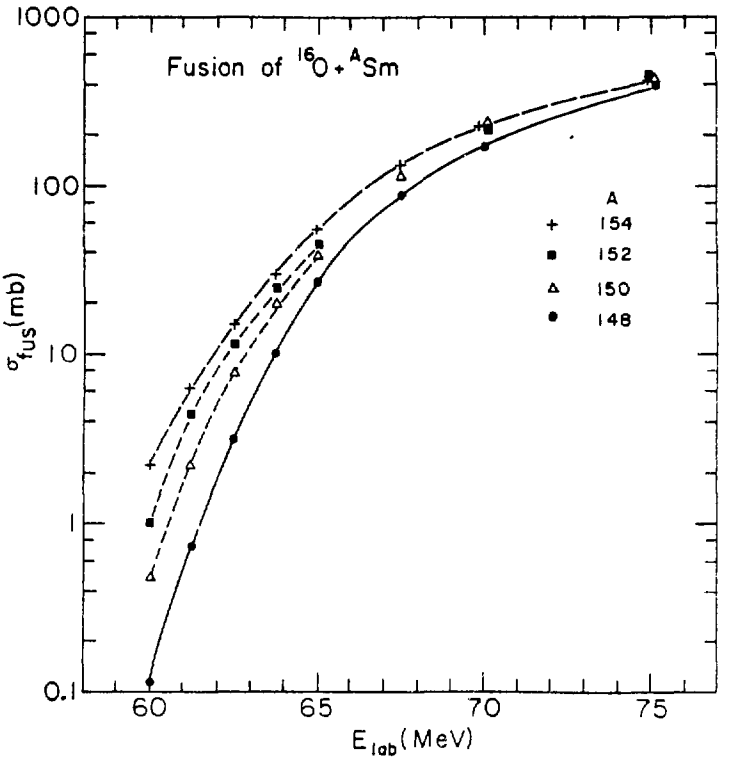


Fig. 42. The fusion cross sections as a function of bombarding energy. The fusion cross sections, similar at energies well above the fusion barrier, vary markedly at low energies with the more deformed isotopes having the larger cross sections. The lines are to guide the eye.

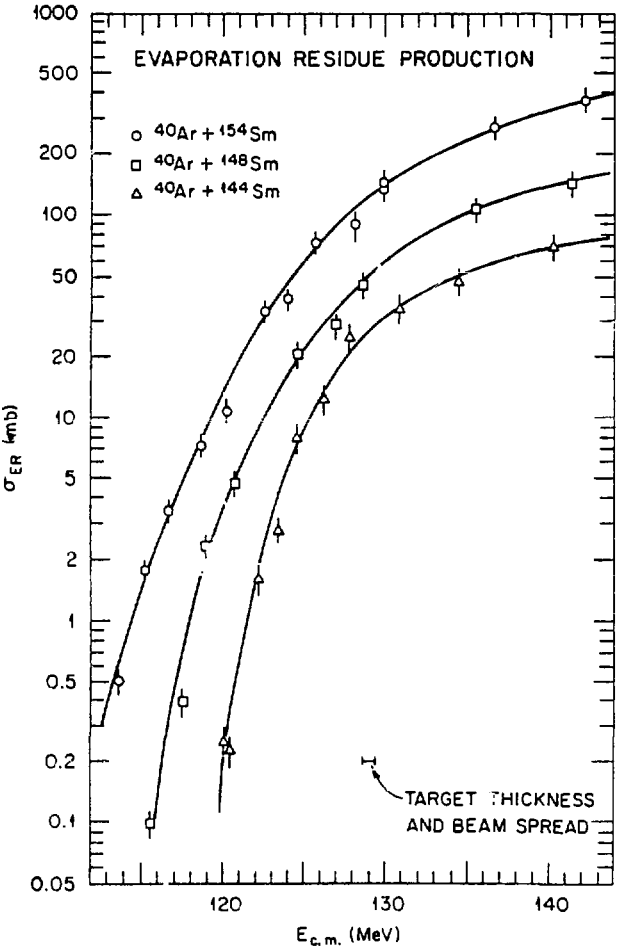


Fig. 43. The measured evaporation residue cross sections for the fusion of $^{40}Ar + ^{144,148,154}Sm$.

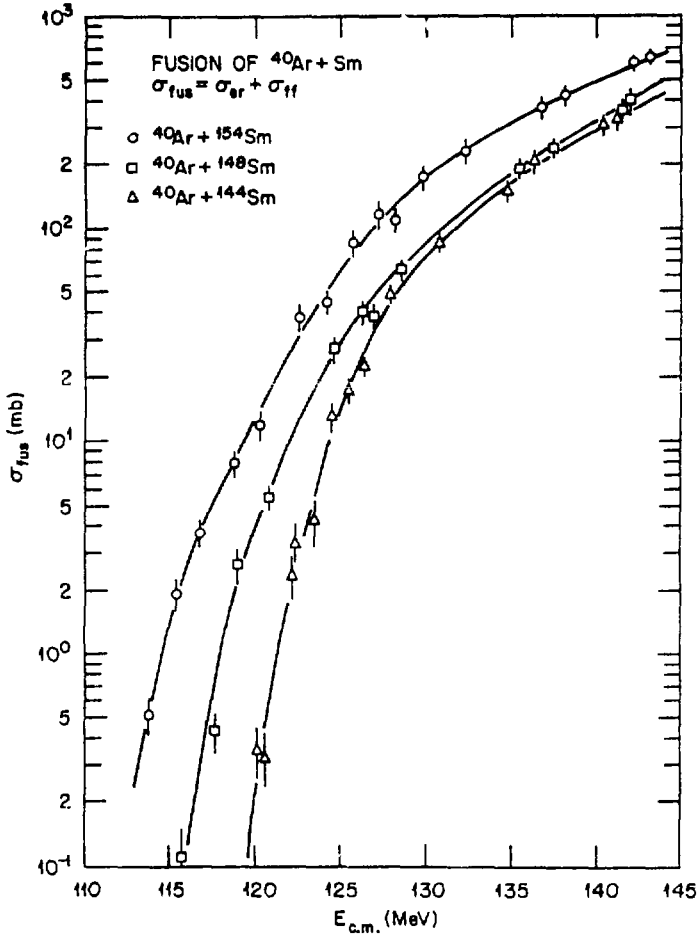


Fig. 44. The measured value of the fusion cross section which is the sum of the cross sections for evaporation residue production and for fusion-fission. A data point is shown at each energy for which either an evaporation residue or a fusion-fission measurement was made. The unmeasured quantity at that energy was obtained by interpolation.

and first $2^+$ states. The pattern of the higher energy levels ($4^+$,$2^{+1}$,$6^+$,etc.) also changes from vibrational to rotational as neutron number increases, with the most rapid change occuring at N = 90 where $^{152}$Sm takes on a recognizably rotational level structure. The parameter $\beta_2$ defined in a rotational model by

$$\beta_2 = [B(E2,0\rightarrow 2)]^{1/2} [3ZR_o^2/4\pi]^{-1},$$

where $R_o = 1.2A^{1/3}$ fm, corresponds approximately to an equilibrium deformation for $^{152,154}$Sm and to a root mean square vibrational amplitude for $^{144}$Sm - $^{150}$Sm. The deviations of the shape of the nuclear surface from sphericity, the motions of the nuclear surface, and the energy and angular momentum which are removed from the relative kinetic energy of target and projectile when these modes become excited - all these factors will influence the fusion cross section above and beyond its dependence on the $A^{1/3}$ variation of the nuclear radius. The problem, then, is how to isolate those factors which are most important in explaining the clear correlation of the fusion cross sections (at subthreshold energies) with the nuclear structure characteristics shown in Fig. 35.

The inclusion of structure effects in the calcualation of fusion cross sections presupposes that the fusion of a spherical projectile with a spherical, structureless target can be calculated sufficiently accurately. This, however, cannot be done on an apriori basis. The reason is that at low energies, the barrier penetrability is extremely sensitive to the nuclear radius (more generally, to the height and shape of the barrier) and this cannot be predicted with sufficient accuracy. Thus, one is forced to make a phenomenological determination from fitting experimental data, and, as Fig. 35 shows, a completely structureless target is not available.

The first approximation which we make in examining the experimental data for $^{16}O$ + Sm is that $^{148}Sm$ is a structureless sphere. Having done this, a real and an imaginary nuclear potential are found which, when inserted into the Schrödinger equation, yield absorption cross sections which reproduce the experimental fusion cross sections for $^{16}O$ + $^{148}Sm$. It is possible to fit the data quite well in this way. The curve drawn to guide the eye in Fig. 42 is indistinguishable from the fit. Once such an empirical spherical potential is fixed, the effect of the static deformation can be included (again, in an approximate way) by replacing the real and imaginary nuclear radii with

$$R \rightarrow R_p + R_T(\theta)$$

where

$$R_T(\theta) = R_T^o\left(1 + \sum_{\lambda=2}^{\infty} \beta_\lambda \, Y_\lambda^o(\theta)\right).$$

Here, $\theta$ specifies the orientation of the axis of symmetry of the deformed nucleus with respect to the direction of the projectile, $Y_\lambda^o$ is the spherical harmonic of order $\lambda$ and $R_T^o$ is the radius of the target in the absence of deformation. The effects of deformation on the Coulomb potential must also be taken into account. The dependence of the combined Coulomb and nuclear potential on $\theta$ is shown in Fig. 45 for $^{16}O$ + $^{154}Sm$ and $\beta_2 = 0.27$, $\beta_4 = 0.054$ and $\beta_6 = -0.018$. These deformation parameters were determined from measurements of $\alpha$-particle inelastic scattering.[80] The barrier penetration problem is then solved for each partial wave at every angle $\theta$ yielding

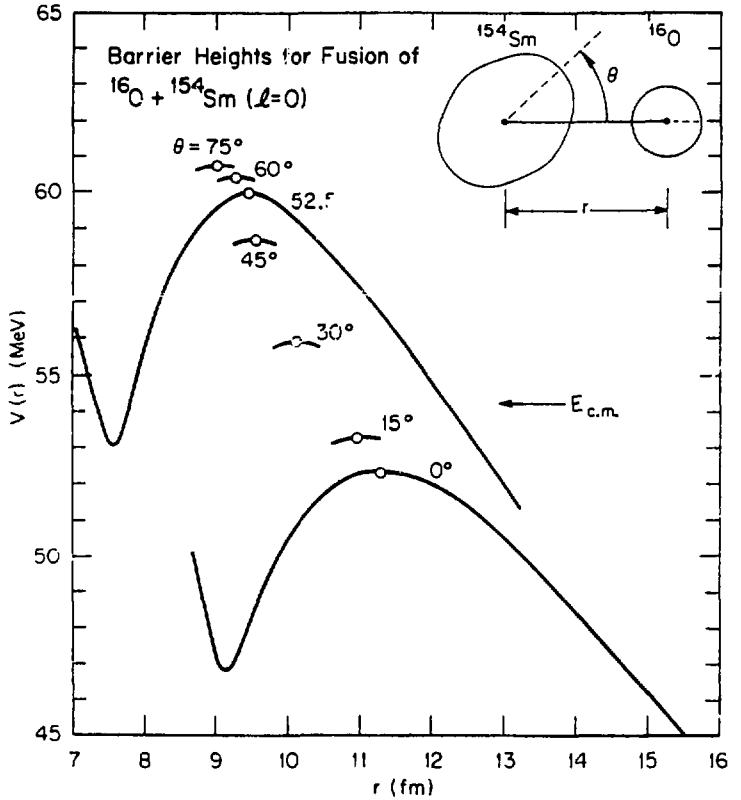


Fig. 45. Barrier heights for the fusion of $^{16}O + ^{154}Sm$. The parameters describing the $\lambda = 2$, 4 and 6 deformations of $^{54}Sm$ were taken from Ref. 80.

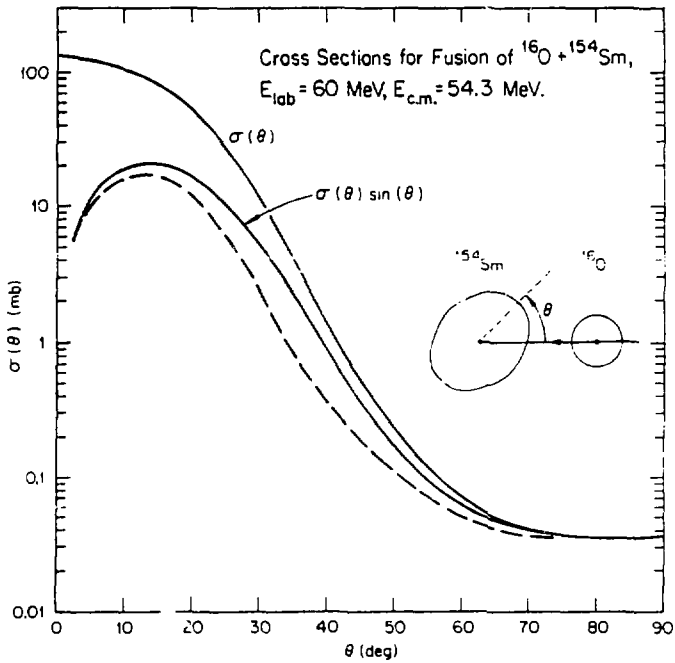


Fig. 46. Fusion cross sections calculated as a function of the orientation of the deformed nucleus with respect to the direction of the projectile. The dashed line includes rotation of the target before fusion.

$$\sigma(\theta) = \pi\lambda^2 \sum_{\ell=0}^{\infty} (2\ell+1)\, T_\ell(\theta)$$

$$\sigma_{fus} = \int_0^{\pi/2} \sigma(\theta) \sin\theta \, d\theta.$$

The quantities $\sigma(\theta)$ and $\sigma(\theta)\cdot\sin\theta$ are shown in Fig. 46. Note that $\sigma(\theta)$ covers four orders of magnitude when the bombarding energy (54.3 MeV, c.m.) is well below the barrier for the spherical case (~60 MeV). Using this prescription for calculating $\sigma_{fus}$, and setting $\beta_4 = \beta_6 = 0$, $\beta_2$ for the other isotopes of Sm can be determined by fitting the excitation functions for fusion. Again, quite good fits can be obtained this way (such as shown by the lines to guide the eye in Fig. 42). The resulting values of $\beta_2$ are given by curve a in Fig. 47. As shown here, the deduced values of $\beta_2$ are much smaller than those values obtained by other methods. Lest this failure rest on the assumption that $\beta_2(^{148}Sm) = 0$, the whole process of determining a spherical potential was repeated, this time fitting the $^{148}Sm$ data under the assumption that $\beta_2 = 0.10$ and then again with $\beta_2 = 0.13$. The results are shown in Fig. 47 and indicate that this simple, static approximation (which might be called the "equivalent sphere" approximation) for including the effects of static deformation is not sufficiently reliable to be used as tool for nuclear structure measurements. It does show, however, that the effects of deformation are significant, and account for the trends of the experimental data shown in Fig. 42.

It is of interest to ask how large is the discrepancy between the predicted and experimental fusion cross sections when the known values of

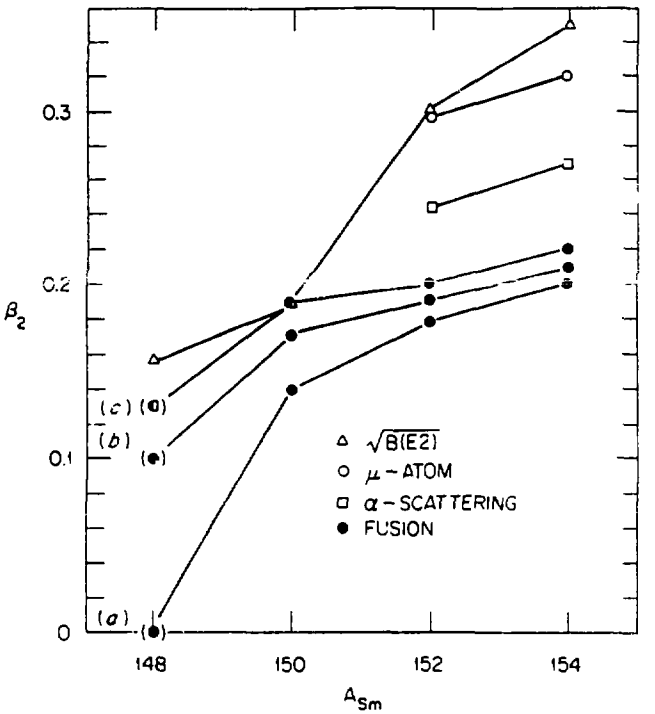


Fig. 47. Values of $\beta_2$ deduced from various types of measurements. The values deduced from fusion depend on the value of $\beta_2$ assumed for $^{148}Sm$.

$\beta_\lambda$ are used. This is shown in Fig. 48 in which the ratio of the cross sections for $^{154}Sm$ and $^{148}Sm$ is plotted. The cross section for $^{154}Sm$ at the lowest energy is predicted to be a factor of three larger than observed experimentally.

Many approximations have been made in arriving at the above classical, static, equivalent-sphere prescription for estimating the effects of deformation. A more complete discussion of these approximations and estimates of their consequences is outside the scope of this report and is presented elsewhere.[78] Suffice it to say that the neglect of dynamic effects seems a likely suspect for part of the discrepancy with the experimental data. Dynamic effects here refer (in classical terms) to 1) the induction of an oblate deformation in the target nucleus by the Coulomb field of the projectile,[81] 2) an induced rotation of the nucleus as the projectile approaches, and 3) the loss of relative kinetic energy associated with each of these. In quantum mechanical language, the coupling of the low-lying vibrational and rotational levels to the ground state allows a dynamic polarization of the deformed target and the diversion of flux into the excitation of these motions.[82]

Some initial estimates of these dynamic effects for the case of 60 MeV $^{16}O + ^{154}Sm$ have been made. A classical estimate of the rotation before fusion yields $\sim 3.5^\circ$ and an excitation energy of $\sim$128 keV.[83] The result is a reduction in the $^{154}Sm$ cross section by about a factor of 1.5. (Recall that a reduction factor of $\sim$3 is needed for agreement.) A quantum mechanical, coupled channels calculation including the $2^+$ and $4^+$ rotational

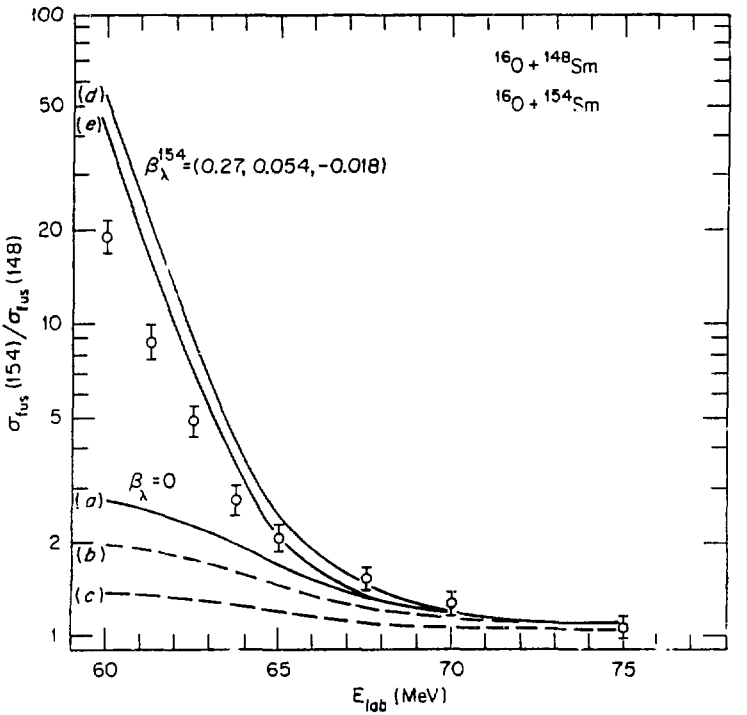


Fig. 48. Ratios of the fusion cross sections for $^{154}Sm$ and $^{148}Sm$. Curve c shows the effects of the lab-cm difference in energy (only), curve b the effects of an $A^{1/3}$ change in the radius (only) and curve a, these effects combined. Spherical nuclei are assumed. Curve d is the static calculation for the indicated deformation parameters. Curve e includes the effects of requiring the deformed nucleus to have the same volume as its spherical equivalent.

levels yields better agreement, the predicted reduction factor for dynamic effects being ~2. Dynamic effects on the fusion of $^{16}O$ with $^{148}Sm$, however, have not yet been included.

Summarizing the $^{16}O$ + Sm fusion results, static effects appear to dominate the changes seen in the fusion cross section for $^{148}Sm$ and $^{154}Sm$, but the inclusion of dynamic effects may be required to produce agreement between predicted and measured cross sections.

An inspection of Fig. 44 shows that the cross sections for $^{40}Ar$ + Sm at low bombarding energies also depend sensitively on the isotopic number and, hence, nuclear structure of the target. Even though the simple static approximation is not adequate for a precise analysis of the data, it may serve as a useful basis for comparing fusion cross sections induced by different projectiles. Such a comparison is of interest because dynamic effects of the type discussed above should become more important and because other degrees of freedom[84] associated with the mass asymmetry of target and projectile might be relevant.

The comparison of the $^{16}O$- and $^{40}Ar$-induced cross sections was done using a different procedure than described above. Instead of integrating the Schrödinger equation for a complex potential, the WKB approximation (Eq. 3) was used. When, for a given partial wave, the c.m. energy was at or above the barrier height, the Hill-Wheeler expression for the barrier penetrability was used. The real nuclear potential was taken to have an exponential shape as given by a proximity-type model.[6] Figure 49a shows the results of fitting $^{16}O$ + $^{148}Sm$ with essentially all parameters free. The result, curve 3, yields $\beta = 0.18$, which is larger than the experimental

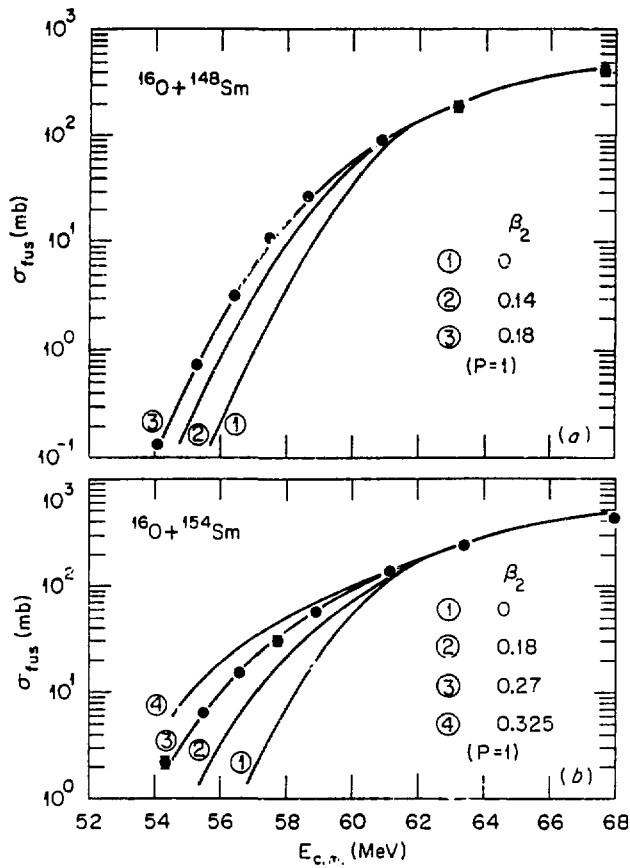


Fig. 49. a) Experimental values of $\sigma_{fus}$ for $^{16}O + ^{148}Sm$. The fits to the data are calculated using a real potential only and the WKB method. b) Same as a) but for $^{16}O + ^{154}Sm$.

value. (There is, of course, an interplay between the parameters describing the spherical potential and the deformation parameter.) Curves 1 and 2 correspond to values of $\beta = 0$ and $\beta = 0.14$. The latter is the experimental value. In Fig. 49b, the results for $^{16}O + {}^{154}Sm$ are shown for values of $\beta = 0.0$, 0.18, 0.27, and 0.33, curves 1-4, respectively. The difference between curve 2 and 3 represents the effect of the different nuclear structures of $^{148}Sm$ and $^{154}Sm$. Note that, here again, the difference in the deduced values of $\beta$ for $^{154}Sm$ and $^{148}Sm$, 0.27 - 0.18 = 0.09, is smaller than the known difference of 0.14 to 0.17.

With the spherical potential thus fixed, and with the change in the potential when $^{40}Ar$ is used instead of $^{16}O$ specified by the proximity formulation, the fusion cross sections for $^{40}Ar$ + Sm may be predicted. This is shown in Fig. 50a by curve 1. While the overall agreement appears rather good, the discrepancy at the lowest bombarding is significant; it occurs in the predictions for the other isotopes as well. It appears that the actual barrier for $^{40}Ar$ + Sm is effectively lowered, or easier to penetrate, than would be expected on the basis of an extrapolation of cross sections with $^{16}O$ projectiles. This may reflect the additional degree of freedom mentioned earlier.[84] In any case it was felt useful to introduce an additional, albeit ad hoc, parameter into the WKB penetrability in order to continue with the comparison of the $^{16}O$ and $^{40}Ar$ data, and to quantitatively compare the fusion of $^{40}Ar$ with the other isotopes of Sm. The WKB penetrability was thus written

$$t = \exp\left(-\frac{2}{\rho}\int_{r_1}^{r_2}\frac{\sqrt{2\mu}}{\hbar}\,[V-E_{c.m.}]dr\right)$$

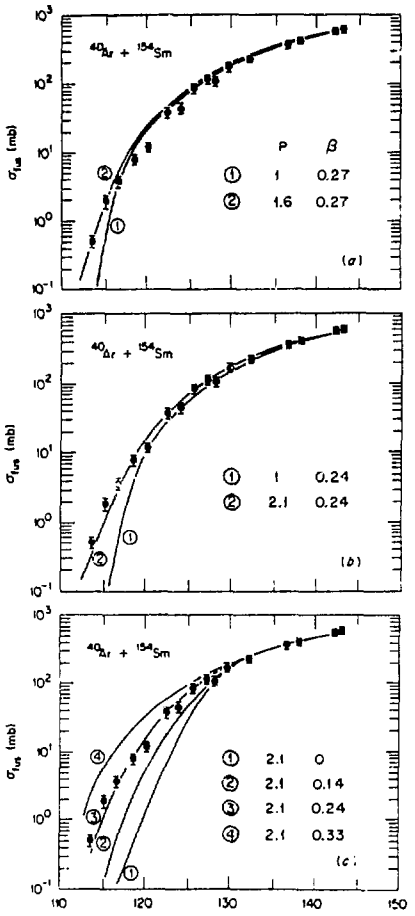


Fig. 50. Experimental values of $\sigma_{fus}$ for $^{40}Ar + ^{154}Sm$
a) Curve 1 is calculated using the ordinary WKB penetrability and parameters fixed by fitting $^{16}O + ^{154}Sm$ (i.e. $\beta_2 = 0.27$). Curve 2 has the parameter p = 1.6 (see text) and all other values the same.
b) Curve 2 is the best fit when both p and β are adjusted.
c) Shows the sensitivity of the predicted cross section to changes in $\beta_2$ when p is fixed.

where for $p > 1$ the penetrability is increased over the usual WKB value (Note that taking $p > 1$ is equilivant to using a smaller reduced mass, $\mu$.) Curve 2 in Fig. 50a shows an excitation function for $\beta = 0.27$ and $p = 1.6$. Allowing both $\beta$ and p to be free parameters yields curve 2 in Fig. 50b; the best fit value of $\beta$ is now 0.24. The sensitivity of the predicted excitation function to the value of $\beta$ when p is held fixed is illustrated in Fig. 50c.

The fits to the data for $^{148}$Sm and $^{144}$Sm are shown in Figs. 51 and 52, respectively. With the value of p fixed at 2.1, best-fit values of $\beta$ are 0 and 0.4 for $^{144}$Sm and $^{148}$Sm, respectively. A new feature emerges with these results, however. This feature many be noted already in the data shown in Fig. 44 - the fusion cross sections for $^{148}$Sm no longer approach (as rapidly) those of $^{154}$Sm as the bombarding energy is raised above the barrier. See Fig. 42 for comparison. Such an effect is not contained in any static model for the fusion cross section and this is reflected in the poor agreement at high energies shown in Figs. 51 and 52. An explanation for this currently is not available. However, it seems reasonable to suspect that this difference is connected with the fact that $^{144,148}$Sm are vibrational whereas $^{154}$Sm is rotational. That this effect first appears with a heavy projectile suggests that it is dynamic in nature because of the much stronger excitation of collective levels by $^{40}$Ar than by $^{16}$O. The dynamic effects which were mentioned previously (and shown to decrease the fusion cross section at low energies) are not in evidence in this comparison of $^{16}$O and $^{40}$Ar. Whereas they should have caused a decrease in the experimental cross section relative to the prediction shown in

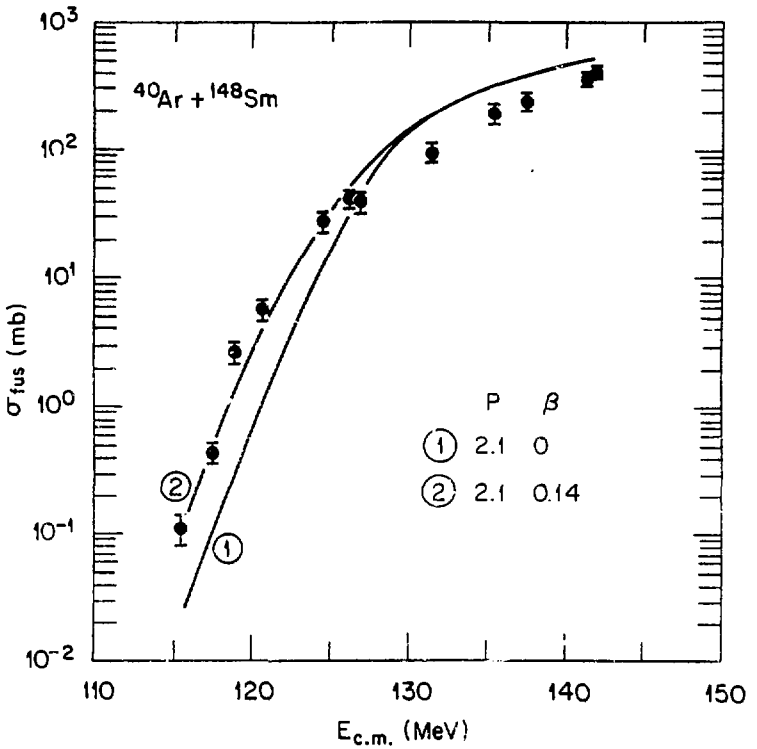


Fig. 51. Experimantal values of $\sigma_{fus}$ for $^{40}Ar + ^{148}Sm$. Both curves have the penetrability factor p = 2.1; curve 1 has $\beta_2 = 0$, curve 2 has $\beta_2 = 0.14$.

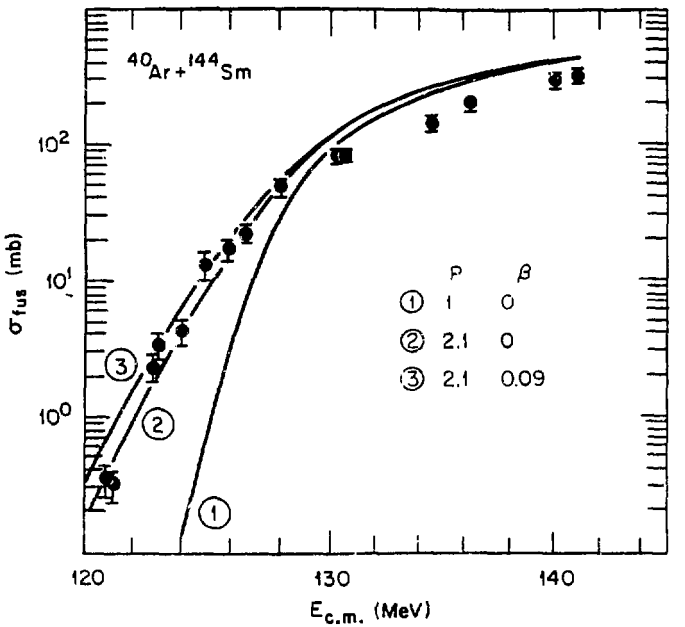


Fig. 52. Experimental values of $\sigma_{fus}$ for $^{40}Ar + ^{144}Sm$. Curve 1 has the penetrability factor p = 1.0, while it is 2.1 for curves 2 and 3.

Fig. 50a by curve 1, the opposite was found to occur. These particular dynamic effects appear to be overshadowed by the possible effect of the additional degree of freedom apparently associated with the size of the projectile.

## E. Section Summary

The availability of precise cross sections for subbarrier fusion of $^{16}O$ and $^{40}Ar$ with the isotopes of Sm makes possible a detailed examination of the current methods of calculating the effect of nuclear deformation on heavy-ion fusion. The approach is to adjust the undetermined parameters of the model (i.e., the potential) to fit the fusion cross sections for one isotope and use this information to make predictions for the other isotopes. Thus, it is mainly the differences in the observed cross sections which are of significance. The equivalent-spheres approximation, which considers the effect of static deformations, accounts for the trends in the data but overestimates the observed differences in the fusion cross sections for the different isotopes when known deformations are used. Equivalently, the deformtions deduced from fitting the fusion data do not vary as widely with isotope number as those derived from B(E2) values. Possible areas for further investigation of these discrepancies include:

(i) the relaxation of the "head-on" approximation

(ii) the inclusion of zero-point motion along with static deformation

(iii) further study of dynamic (i.e., coupled-channels) effects.

Calculations (both classical and quantum mechanical estimates) suggest that these effects should not be neglected in comparing the fusion cross sections for vibrational and rotational nuclei. While most of the observed differences can be understood in terms of static deformation, the level of comparison with the data is now sufficiently precise that the dynamic effects could account for as much as half of the remaining discrepancy. Throughout this analysis it has been assumed that the empirical adjustment of a potential to fit the data for one isotope effectively normalizes out for the other isotopes any effects which cannot be described by a one-dimensional potential, thus enabling the isolation of a deformation effect. While there is no way at the moment to quantitatively check this assumption, it can only be noted that the assumption should be better, the lighter the projectile.

The nature of fusion process seems affected by the size of the projectile in ways not consistent with the expected changes in nuclear potential and reduced mass of the system. These inconsistencies appear at both low and high energies in the $^{40}Ar$ + Sm data. One way of interpreting the observations for $^{40}Ar$ + Sm at low energies is in terms of an additional degree of freedom in the specification of the nuclear potential for $^{40}Ar$ + Sm (e.g. an elongation or necking-in coordinate).[84] Recent analyses of other fusion data with heavier projectiles also indicate that more than one dimension (the separation of the nuclei) may be requried to adequately describe barrier penetration.[85,86]

This area of study is ripe for theoretical input. There are a number of ways of treating the dynamics of the problem and of incorporating the nuclear structure information (static deformation, coupled channels, zero point motion of the ground state[87].) Equally important, there are reasonably precise experimental data now available to test these theories. Subbarrier measurements of fusion cross sections for other systems e.g. $^{16}O$ + Sn (Ref. 88) Ni + Ni (Ref. 89) and $^{32}S$ + Sm (Ref. 90) are in progress, and a series of measurements continues at G.S.I. using a variety of techniques.[91] New theoretical methods for understanding these phenomena would provide important motivation and guidance for future experiments

## VI. Concluding Remarks

The approach in these lectures has been to examine experimental data in which the mass and charge of the target and/or projectile were varied by small amounts. Three different types of experiments were discussed, each with their own experimental method, and were compared with predictions for $\sigma_{fus}$ which incorporated only the most simple approximations and assumptions for the fusion mechanism. In each of these three cases we saw that the experimental data exhibited phenomena well outside the variations expected on the basis of the fusion of spherical nuclei having no structure or internal degrees of freedom.

Sub-Coulomb cross sections are extremely sensitive to the interaction potential because the integral over the wave number is in the argument of an exponential (Recall Eq. 3). This fact was exploited to study the effect of a static nuclear deformation on the fusion of $^{16}O$ and $^{40}Ar$ with the

isotopes of samarium. The variations in $\sigma_{fus}(E)$ with neutron number of the target were found to be quite regular and systematic although somewhat smaller than expected when deformation effects were included in a simple barrier penetration model. This regularity is in contrast to what was observed with light nuclei fusing with light nuclei. This is perhaps not surprising since it is reasonable to expect that the effect of a valence nucleon on the fusion process will be largest when the total number of nucleons in the nucleus is small. About half of the systems studied agreed with a standard prediction and the remainder showed deviations (up to a factor of two) in the form of a broad structure, of an MeV or more in width, in the energy - averaged variation of $\sigma_{fus}(E)$. There is at present no comprehensive explanation, neither qualitative nor quantitative, for this behavior. It appears likely that the origin of the explanation must be found within the context of a microscopic model which incorporates the effect of individual nucleons on the absorptive part of the interaction potential. Clues to this explanation might be sought in an empirical correlation of the energy dependence of $\sigma_{fus}$ with properties of the colliding nuclei such as the spectrum of low-lying excitations, Q-values for transfer reactions or for compound nucleus formation, occupied shell model orbitals, etc.

When light nuclei collide at high bombarding energies, the fusion process is dominated by a delicate balance between attractive nuclear forces, repulsive centrifugal forces, and the non-conservative forces causing the dissipation of relative kinetic energy. In a balanced situation such as this, it is plausible that individual nucleons might play an important role in variations

of $\sigma_{fus}$ from one system to another. When high angular momenta are involved, the properties of both the entrance channel and the compound nucleus may be important in determining the size of the fusion cross section. Experiments must be chosen in order to determine if possible which of these properties is the limiting factor in a particular energy region. Studies of different entrance channels which populate the same compound system (i.e. the same Z and A) are valuable in this respect. Comparisons of $^{10}B + ^{16}O$ and $^{12}C + ^{14}N$ which populate $^{26}Al$ indicate that the compound nucleus is the limiting factor once a maximum angular momentum $J_c \sim 27\ \hbar$ is reached. At this point further increases in bombarding energy cause reductions in $\sigma_{fus}$ ($\propto 1/E$) and corresponding increases in $\sigma_{direct}$. This limit, $27\hbar$, is consistent with the predictions of the rotating liquid drop model. At lower bombarding energies the entrance channel seems to be the limiting factor in so far as different critical angular momenta are reached at the same excitation energy in the compound nucleus. (This is especially apparent in the existing data for $^{10}B + ^{14}N \rightarrow ^{24}Mg$ and $^{12}C + ^{12}C \rightarrow ^{24}Mg$). Nevertheless, the trends of $\sigma_{fus}$ from one system to the next correlate well with the Q-value for compound nucleus formation and this has led to the concept of a statistical or effective Yrast line as a mechanism for limiting $\sigma_{fus}$. The delineation of entrance channel and compound nuclear effects is just beginning and we may expect to see more progress in the future as new experimental data become available.

I would like to conclude by drawing attention first to some immediate needs for experimental work. The experimental situation for $^{16}O + ^{16}O$ is in great need of clarification. Because of its closed-shell nature, this system will always be of special importance for theoretical

work, and the current spread in experimental values (Table I) makes a definitive comparison with theory all but impossible. There are systematic errors, apparently peculiar to this system, which may only be found by the different experimental groups performing the others' measurements. On the theoretical side, systematic analyses of the experimental data in terms of deformation ($^{12}C$ and $^{20}Ne$ have large deformations) analogous to those done for the heavier systems might prove interesting.

Subbarrier fusion measurements of spherical nuclei with spherical nuclei (e.g. $^{16}O$ + Ca, Sn, or Pb) would be most useful. (In some respects these measurements should be understood before attempting to study more complex phenomena such as the effect of deformation). The effect of vibrational motion in the ground state and in excited states is yet to be studied in any detail. Similarily, odd-A nuclei should be included along with the even-even isotopes. From systematic measurements of subbarrier cross sections over a wide range of projectile and target mass one may hope to gain additional evidence for the phenomenon of neck formation in the fusion process.

Measurements of $\sigma_{fus}$ at high energies are still relatively few in number. The generality of the liquid drop limit for all nuclear systems is perhaps taken for granted, but this does not remove the need for additional experimental verification after the phenomenon has been observed in one system (viz $^{26}Al$). In fact, it is important that the $^{24}Mg$ system be studied at higher energies, and that the $^{10}B$ + $^{14}N$ and $^{12}C$ + $^{12}C$ data be subjected to identical analysis, in order to clarify

the situation viz a vis the liquid drop limit. Measurements on heavier targets[92,-95] have demonstrated that substantial residue-like yields are associated with incomplete momentum and mass transfer. So far, analogous processes have not been detected in residue-like yields from $^{12}C + ^{14}N$ and $^{10}B + ^{16}O$. In these cases (in contrast to heavier targets) the effects of incomplete fusion should be experimentally observable in the energy spectrum of residues. Thus the incomplete fusion yield, to the extent that it is present, apparently has been included, as it should be, with the direct or peripheral reactions. Further study of this question using both singles and coincidence measurements is needed.

## VII. Acknowledgements

The experiments on heavy-ion fusion in which I have been involved were done at a number of laboratories and in collaboration with many people. It is with pleasure and gratitude that they are acknowledged here.

California Institute of Technology

R. A. Dayras

Z. E. Switkowski

R. M. Wieland

Oak Ridge National Laboratory

J. Biggerstaff

Y. D. Chan

D. DiGregorio

R. A. Dayras

J. L. C. Ford Jr.

J. Gomez del Campo

E. E. Gross

D. C. Hensley

M. E. Ortiz

D. Shapira

A. H. Snell

P. H. Stelson

Weizmann Institute of Science

Y. Eisen

S. Kaplanis

D. Pelte

U. Smilansky

I. Tserruya

Gesellschaft fuer Schwerionenforschung

K. D. Hildenbrand

J. V. Kratz

R. Lucas

J. Poitou

W. Reisdorf

G. Wirth

Lawrence Berkeley Laboratory

C. Olmer

M. Zisman

## References


1. G. R. Satchler and W. G. Love, Phys. Lett. 65B, 415 (1976).
2. J. Maruhn and W. Greiner, A. Phys. 251, 431 (1972).
3. D. Glas and U. Mosel, Phys. Letts. 49B, 301 (1974), Nucl. Phys. A264, 268 (1976).
4. H. Flocard, S. E. Koonin, and M. S. Weiss, Phys. Rev. C17, 1682 (1978). P. Bonche, B. Grawmaticos and S. Koonin, ibid. p. 1700.
5. R. Bass, Phys. Letts. 47B 139 (1974).
6. J. Blocki, J Randrup and C. F. Tsang, Ann. Phys. 105, 427 (1977).
7. P. R. Christensen and Z. F. Switkowski, Nucl. Phys A280, 205 (1977).
8. J. Wilczynski, Nucl. Phys. A216, 386 (1973).
9. J. Galin, D. Guerreau, M. Lefort, and X. Tarrago, Phys. Rev. C9, 1018 (1974)
10. D. Glas and U. Mosel, Phys. Rev. C10, 2620 (1974), Nucl. Phys. A237, 429 (1975).
11. C. H. E. Gross and H. Kalinowski, Phys. Letts. 48B, 302 (1974).
12. J. K. Birkelund, L. E. Tubbs, J. R. Huizenga, J. N. De and D. Sperber, Phys. Rep. C45, 108 (1979).
13. W. U. Schröder and J. R. Huizenga, Ann. Rev. Nucl. Sci. 27, 465 (1977).
14. T. Tamura, Rev. Mod. Phys. 37, 679 (1965)
15. D. Pelte and U. Smilansky, Phys. Rev. C19, 2196 (1979).
16. L. C. Vaz and J. M. Alexander. preprint (1980).
17. Y. Eisen, I. Tserruya, Y. Eyal, Z. Fraenkel and M. Hillman, Nucl. Phys. A291, 459 (1977).

18. C. Rolfs and H. P. Trautvetter, Ann. Revs. Nucl. Sci. 28, 115 (1978).

19. R. A. Dayras, R. G. Stokstad, Z. E. Switkowski and R. M. Wieland, Nucl. Phys. A265, 153 (1976).

20. M. D. High and B. Cujec, Nucl. Phys. A259, 513 (1976).

21. R. A. Dayras, R. B. Stokstad, Z. E. Switkowski, and R. M. Wieland, Nucl. Phys. A261, 478 (1976).

22. M. D. High and B. Cujec, Nucl. Phys. A278, 149 (1977).

23. Z. E. Switkowski, Shiu-Chin Wu, J. C. Overley and C. A. Barnes, Nucl. Phys. A289, 236 (1977)

24. R. G. Stokstad, Z. E. Switkowski, R. A. Dayras and R. M. Wieland, Phys. Rev. Letters 37, 888 (1976), R. G. Stokstad, Proc. Topical Conf, on Heavy Ion Collisions, Fall Creek Falls, Tenn. (1977) ORNL report: CONF 770602 p. 22.

25. H. C. Cheung, M. D. High and B. Cujec, Nucl. Phys. A296, 333 (1978).

26. Z. E. Switkowski, R. M. Wieland and A. Winther, Phys. Rev. Lett. 33, 840 (1974).

27. M. Mazarakis and W. E. Stephens, Phys. Rev. C7, 1280 (1973).

28. K. U. Kettner, H. Lorenz-Wirzba, C. Rolfs, and H. Winkler, Phys. Rev. Letts. 38, 337 (1977).

29. Z. E. Switkowski, R. G. Stokstad, and R. M. Wieland, Nucl. Phys A279, 502 (1977).

30. B. Cujec, and C. A. Barnes, Nucl. Phys. A266, 461 (1976).

31. Z. E. Switkowski, R. G. Stokstad and R. M. Wieland, Nucl. Phys. A274, 202 (1976).

32. H. Spinka and H. Winkler, Nucl. Phys. A233, 456 (1974).

33. G. Hulke, C. Rolfs, and H. P. Trautvetter, submitted to Z. Physik (1980).

34. D. G. Kovar et. al. Phys. Rev. C20, 1305 (1979).

35. I. Tserruya, Y. Eisen, D. Pelte, A. Gavron, H. Oeschler, D. Berndt and H. L. Harney, Phys. Rev. C18, 1688 (1978).

36. J. J. Kolata, R. M. Freeman, F. Haas, B. Heusch and A. Gallmann, Phys. Rev C19, 2237 (1979).

37. V. K. C. Cheng, A. Little, H. C. Yuen, S. M. Lazarus, and S. S. Hanna, Nucl. Phys. A322, 168 (1979).

38. S. C. Wu and C. A. Barnes, to be published.

39. R. Wieland and G. R. Satchler, private communication.

40. S. J. Krieger and K. T. R. Davies, Phys. Rev. C20, 167 (1979).

41. J. Y. Park, W. Greiner and W. Scheid, Phys. Rev. C21, 958 (1980).

42. C. von Charzewski, V. Hinzdo and C. Toepffer, Proc. Int. Conf. on Dynamical Properties of Heavy-Ion Reactions, Johannesburg, S. Afr., J. Phys. 1 222 (1978).

43. D. L. Hanson, R. G. Stokstad, K. A. Erb, C. Olmer, M. W. Sachs and D. A. Bromley, Phys. Rev. C9, 1760 (1974).

44. S. Cohen F. Plasil and W. J. Swiatecki, Ann Phys. (NY) 82, 557 (1974).

45. P. Sperr et. al., Phys. Rev. Lett. 36, 405 (1976), 37, 321 (1976).

46. M. Conjeaud, S. Gary, S. Harar and J. P. Wieleczko, Nucl. Phys. A309, 515 (1978).

47. R. G. Stokstad, J. Gomez del Campo, J. A. Biggerstaff, A. H. Snell and P. H. Stelson, Phys. Rev. Letts. 36, 1529 (1976).

48. R. G. Stokstad, R. A. Dayras, J. Gomez del Campo, P. H. Stelson, C. Olmer, and M. S. Zisman, Phys. Letts 70B, 289 (1977).

49. J. Gomez del Campo, R. G. Stokstad, J. A. Biggerstaff, R. A. Dayras, A. H. Snell and P. H. Stelson, Phys. Rev. C19, 2170 (1979).

50. J. Gomez del Campo, R. A. Dayras, J. A. Biggerstaff, D. Shapira, A. H. Snell, P. H. Stelson, and R. G. Stokstad, Phys. Rev. Lett. 43, 26 (1979).

51. R. G. Stokstad, D. C. Hensley and A. H. Snell, Nucl. Inst. Meth. 141, 499 (1977).

52. D. Shapira, R. A. Dayras, J. L. C. Ford, Jr., J. Gomez del Campo, A. H. Snell, P. H. Stelson and R. G. Stokstad Nucl. Instrm. Meth. 163, 325 (1979).

53. LILITA - A Monte Carlo Statistical Model Code, J. Gomez del Campo and R. G. Stokstad. ORNL TM-7295

54. D. Digregorio et. al. private communication.

55. R. G. Stokstad, R. M. Wieland, G. R. Satchler, C. B. Fulmer, D. C. Hensley, S. Raman, L. D. Rickertsen, A. H. Snell and P. H. Stelson. Phys. Rev. C20, 655 (1979).

56. M. E. Ortiz, Y. D. Chan, D. Digregorio, J. Gomez del Campo, D. Shapira et. al., private communication.

57. J. P. Wieleczko et. al., private communication.

58. R. J. Parks, S. T. Thornton, L. C. Dennis and K. R. Cordell, preprint.

59. M. N. Namboodiri, E. T. Chulick, and J. B. Natowitz, Nucl. Phys. A263, 491 (1976).

60. R. Vandenbosch, preprint.

61. J. P. Wieleczko, S. Harar, M. Conjeaud and F. Saint-Laurent, submitted to Phys. Letts. S. Harar Proc. Int. Conf. Berlin, Oct. 79.

62. S. M. Lee, T. Matsuse and A. Arima, Phys. Rev. Letters, 45, 165 (1980).

63. D. Glas and U. Mosel, Phys. Letts 78B, 9 (1978); M. Diebel, D. Glas, U. Mosel, and H. Chandra, Nucl. Phys. A333, 253 (1980).

64. R. Vandenbosch, Phys. Letts. 87B 183 (1979), R. Vandenbosch a A. J. Lazzarini, preprint.

65. D. Shapira, R. G. Stokstad and D.A. Bromley, Phys. Rev. C10 1063 (1974).

66. A. Gilbert and A. G. W. Cameron, Can. J. Phys. 43 1446 (1965).

67. O. Tanimura, Phys. Letts. 90B, 50 (1980).

68. R. Vandenbosch et. al., Phys. Rev. Lett. 33, 842 (1974).

69. S. Kox, A. J. Cole, and R. Ost, Phys. Rev. Letters 44, 1204 (1980), A. J. Cole, N. Longequene, J. Menet, J. J. Lucas, R. Ost, and J. B. Viano, Nucl. Phys. A341, 284 (1980).

70. F. Saint Laurent, M. Conjeaud, S. Harar, J. M. Loiseaux, J. Menet, J. B. Biano, Nucl. Phys. A327 517 (1979).

71. B. Fernadez, C. Gaarde, J. S. Larsen, S. Pontoppidan, F. Videbaek, Nucl. Phys. A306, 259 (1978).

72. J. Barrette, O. Hansen, M. J. Levine, C. J. Lister, and H. E. Wegner, Contr. to Int. Conf. on Nuclear Physics, Berkeley, 1980.

73. M. E. Ortiz, Y. D. Chan, J. Gomez del Campo, et. al.

74. R. Vandenbosch and A. J. Lazzarini, private communication.

75. I. Tserruya, private communication.

76. Y. D. Chan, R. A. Dayras, D. Shapira, J. Gomez del Campo, D. Digregorio, private communication.

77. R. G. Stokstad, Y. Eisen, S. Kaplanis, D. Pelte, U. Smilansky, and I. Tserruya, Phys. Rev. Letters 41, 465 (1978); Phys. Rev. C21, 2427 (1980).

78. R. G. Stokstad and E. E. Gross, submitted to Phys. Rev. C.

79. R. G. Stokstad, W. Reisdorf, K. D. Hildenbrand, J. V. Kratz, G. Wirth, R. Lucas and J. Poitou, Z. Phys. 295, 269 (1980).

80. D. L. Hendrie, N. K. Glendenning, B. G. Harvey, O. N. Jarvis, H. H. Duhm, J. Sandinos, and J. Mahoney, Phys. Letts. 26B, 127 (1968).

81. P. W. Riesenfeldt and T. D. Thomas, Phys. Rev. C2, 711 (1970).

82. H. Freiesleben and J. R. Huizenga, Nucl. Phys. A224, 503 (1974).

83. S. Levit, private communication (1978).

84. T. Kodama, R.A.M.S. Nazareth, P. Moller, and J. R. Nix, Phys. Rev. C17, 111 (1978).

85. B. Sikora, J. Bisplinghoff, W. Scobel, M. Beckerman, and M. Blann, Phys. Rev. C20, 2219 (1979).

86. L. C. Vaz, J. M. Alexander, and G. R. Satchler, Phys. Rev. (submitted).

87. H. Esbensen, A. Winther, R. A. Broglia, and C. H. Dasso, Phys. Rev. Letts. 41, 296 (1978); private communication (1979).

88. D. M. Moltz, private communication

89. M. Beckerman, et. al., preprint 1980.

90. B. Back, et. al. preprint 1980.

91. W. Reisdorf, private communication.

92. K. Siwek-Wilczynska, E. H. du Marchie van Voorthuysen, J. van Panta, R. H. Siemssen and J. Wilczynski, Phys. Rev. Lett. 42, 1559 (1979).

93. D. R. Zolnowski, H. Yamada, S. E. Cala, A. C. Kahler, and T. T. Sugihara, Phys. Rev. Lett. 41, 92 (1978).

94. K. A. Geoffroy, D. G. Sarantites, M. L. Halbert, D. C. Hensley, R. A. Dayras and J. H. Barker, Phys. Rev. Letters 43 1303 (1979).

95. P. Gonthier, H. Ho, M. N. Namboodiri, L. Adler, J. B. Natowitz, S. Simon, K. Hagel, R. Terry and A. Khodai, Phys. Rev. Letters 44, 1387 (1980).